Weighing nanoparticles in solution at the attogram scale

Selim Olcum[a,b,1], Nathan Cermak[c,1], Steven C. Wasserman[a], Kathleen S. Christine[d,e], Hiroshi Atsumi[f], Kris R. Payer[g], Wenjiang Shen[h], Jungchul Lee[i], Angela M. Belcher[a,b,f], Sangeeta N. Bhatia[b,d,e,j,k], and Scott R. Manalis[a,b,c,l,2]

Departments of [a]Biological Engineering, [f]Materials Science and Engineering, [j]Electrical Engineering and Computer Science, and [l]Mechanical Engineering, [b]Koch Institute for Integrative Cancer Research, [c]Computational and Systems Biology Initiative, [d]Harvard–MIT Health Sciences and Technology, [e]Institute for Medical Engineering and Science, and [g]Microsystems Technology Laboratories, Massachusetts Institute of Technology, Cambridge, MA 02139; [h]Innovative Micro Technology, Santa Barbara, CA 93117; [i]Department of Mechanical Engineering, Sogang University, Seoul 121-742, Korea; and [k]Howard Hughes Medical Institute, Cambridge, MA 02139

Edited by Alexis T. Bell, University of California, Berkeley, CA, and approved December 13, 2013 (received for review October 4, 2013)

Physical characterization of nanoparticles is required for a wide range of applications. Nanomechanical resonators can quantify the mass of individual particles with detection limits down to a single atom in vacuum. However, applications are limited because performance is severely degraded in solution. Suspended micro- and nanochannel resonators have opened up the possibility of achieving vacuum-level precision for samples in the aqueous environment and a noise equivalent mass resolution of 27 attograms in 1-kHz bandwidth was previously achieved by Lee et al. [(2010) *Nano Lett* 10(7):2537–2542]. Here, we report on a series of advancements that have improved the resolution by more than 30-fold, to 0.85 attograms in the same bandwidth, approaching the thermomechanical noise limit and enabling precise quantification of particles down to 10 nm with a throughput of more than 18,000 particles per hour. We demonstrate the potential of this capability by comparing the mass distributions of exosomes produced by different cell types and by characterizing the yield of self-assembled DNA nanoparticle structures.

nanoparticle characterization | NEMS | microfluidics | mechanical oscillators

Many aspects of engineered and naturally occurring aqueous nanoparticles with diameters below 50 nm remain unexplored. Particles in this size range play a central role in a wide range of applications, including targeted drug delivery (1, 2), therapeutic protein formulation (3, 4), and the study of intracellular signaling via exosomes (5). In all these cases, function is strongly correlated to particle size and concentration. Established methods for characterizing these particles such as electron microscopy, dynamic light scattering (DLS), and disk centrifugation can determine the size of particles down to the nanometer scale, but generally have limitations when it comes to heterogeneous samples, throughput, measuring concentration, or ease of use (6–8). Miniaturized resistive pulse sensors (9, 10) can quantify size, heterogeneity, and concentration of particles bigger than about 50 nm, but require high salinity, which is an important consideration when characterizing biological nanoparticles, such as protein aggregates.

Nanomechanical resonators in vacuum can characterize nanoparticles down to a single atom (11, 12) or protein (13, 14), but perform poorly when immersed in solution. Resonators with embedded fluidic channels, known as suspended micro- and nanochannel resonators (15–17) (SMRs and SNRs), exploit the extreme sensitivity of measurement in vacuum, while measuring particles in solution. Although performance of nanomechanical resonators in vacuum has been studied extensively (11, 12, 18–20), the practical detection limits of SNRs have only received theoretical treatment to date (21). A proof-of-concept SNR implementation detected gold nanoparticles with a buoyant mass of 77 attograms (ag) at low throughput (bandwidth) (17), far above the thermomechanical noise limit and insufficient to detect lighter particles of biological interest, such as exosomes. The performance achieved here approaches the thermomechanical noise limit, allowing us to measure the mass distributions of 10-nm gold particles and exosomes, which range in size from 30 to 100 nm (22).

Device Design and Evaluation

SNR systems work by measuring the resonant frequency of a microcantilever suspended in vacuum, which is extremely sensitive to changes in mass. A feedback loop keeps the cantilever oscillating at its resonant frequency while particles in solution flow through a U-shaped microfluidic channel running the length of the cantilever. As a particle passes through the cantilever, the cantilever mass transiently changes by the particle's buoyant mass (particle mass minus mass of the fluid it displaces), inducing a brief detectable change in the oscillation frequency. Thus, the signal magnitude depends on the difference between the fluid density and the particle density, but all other solvent properties, such as salinity, can be varied depending upon the desired sample environment.

Improving SNRs to achieve attogram-scale resolution with this method requires increasing mass sensitivity and reducing frequency noise. Mass sensitivity is proportional to the resonant frequency of the cantilever and inversely proportional to its mass (23), so we designed and fabricated a family of SNRs with reduced masses and increased resonant frequencies (Table 1). The mass of the smallest cantilever design (type 3 in Table 1) is nearly 3× lower than previous designs (17) (type 0), with a resonant frequency nearly 5× greater, resulting in up to 14-fold sensitivity improvements. Moreover, frequency noise decreases as oscillation amplitude increases, until Duffing-type mechanical nonlinearity

Significance

Naturally occurring and engineered nanoparticles (e.g., exosomes, viruses, protein aggregates, and self-assembled nanostructures) have size- and concentration-dependent functionality, yet existing characterization methods in solution are limited for diameters below ~50 nm. In this study, we developed a nanomechanical resonator that can directly measure the mass of individual nanoparticles down to 10 nm with single-attogram (10^{-18} g) precision, enabling access to previously difficult-to-characterize natural and synthetic nanoparticles.

Author contributions: S.O., J.L., A.M.B., S.N.B., and S.R.M. designed research; S.O., N.C., S.C.W., K.S.C., and H.A. performed research; K.R.P. and W.S. contributed new reagents/analytic tools; S.O. and N.C. analyzed data; and S.O., N.C., S.C.W., and S.R.M. wrote the paper.

Conflict of interest statement: S.R.M. declares competing financial interests as a cofounder of Affinity Biosensors, which develops techniques relevant to the research presented.

This article is a PNAS Direct Submission.

[1]S.O. and N.C. contributed equally to this work.

[2]To whom correspondence should be addressed. E-mail: scottm@media.mit.edu.

This article contains supporting information online at www.pnas.org/lookup/suppl/doi:10.1073/pnas.1318602111/-/DCSupplemental.

Table 1. Dimensions and theoretically calculated properties of the suspended nanochannel resonators

Type	Length, μm	Thickness, μm	Width, μm	Channel height, nm	Channel width, μm	Resonant frequency, MHz	Stiffness, N/m	Mass, pg	Sensitivity, mHz/ag	δm_{th} (ag)
Type 0	50	1	10	400	2	0.589	3.5	1,059	−1.15	2.7
Type 1	37.5	1	7.5	400	1	1.03	6.3	615	−3.47	1.2
Type 2	27	1	7.5	400	1	1.99	16.9	443	−9.3	0.5
Type 3	22.5	1	7.5	400	1	2.87	29.1	369	−16.1	0.3

Properties were calculated assuming the cantilevers are filled with water. The thermomechanical limit of mass resolution (δm_{th}) is the Allan deviation of thermal energy-induced frequency fluctuations of the cantilever motion (28, 29) at gate time of 1 ms, when the cantilever is driven at the onset of mechanical nonlinearity (21) (*SI Appendix*, sections 3 and 4).

is observed (24). To reach optimal oscillation amplitudes, we used piezoceramic actuators to drive the cantilevers (Fig. 1*A*). Driving cantilevers beyond their linear range caused spring stiffening, which was indicated by a right shift of the open-loop frequency response curves (Fig. 1*B*). In this work, all resonators were driven at their onsets of nonlinearity to achieve the best frequency stability. It was not possible to drive resonators into this regime with the electrostatic actuation that was used in the previous systems (15, 17).

In the new SNR system (*SI Appendix*, Fig. S1), an optical lever setup similar to one previously described (17) detects the cantilever's motion. The cantilever displacement signal acquired from a photodetector is phase-shifted via an adjustable delay on a field-programmable gate array (FPGA) and then amplified and fed back to a high-current amplifier driving a piezoceramic actuator. In the vicinity of the resonant frequency, intrinsic thermomechanical motion of the cantilever is the dominant source of noise on the photodetector output (*SI Appendix*, Fig. S2). The frequency of the oscillation is measured on the FPGA by digitally mixing the cantilever position signal down to 1 kHz and period counting using a 100-MHz clock.

To characterize the noise present in the frequency measurements of SNRs, we measured the oscillation frequency noise for different cantilevers (*SI Appendix*, Table S1) filled with ultrapure deionized water. We calculated the Allan deviations (25) (*Methods*) as a function of averaging (gate) times as shown in Fig. 2*A*, which is a common metric for oscillator noise. The Allan deviation of the overall oscillator system ranges from 4 to 8 parts per billion (ppb) at room temperature (without temperature control) using measurement rates of 5–1,000 Hz, which is the frequency range of interest for higher throughput. For type 2 and 3 cantilevers, this noise magnitude is equivalent to less than 1 ag (10^{-21} kg or 600 kilodaltons), which is demonstrated in Fig. 2*B* as mass-equivalent Allan deviation. The increasing noise at low gate times for type 0 and 1 cantilevers corresponds to white frequency noise, the flat region at the center for all cantilever types corresponds to the flicker (1/f) frequency noise and the ramp in the higher averaging durations corresponds to Brownian frequency noise and long-term frequency drift of the oscillators (26, 27).

To quantify the potential for further reductions in the noise level, we calculated the ultimate limit of frequency stability imposed by intrinsic thermomechanical fluctuations (28, 29) (*SI Appendix*, sections 3 and 4) for resonators driven at their onset of nonlinearity (21) (dashed lines in gray region of Fig. 2*A*). Measured frequency stability values at 1-ms gate time are 1.8- to 3.4-fold

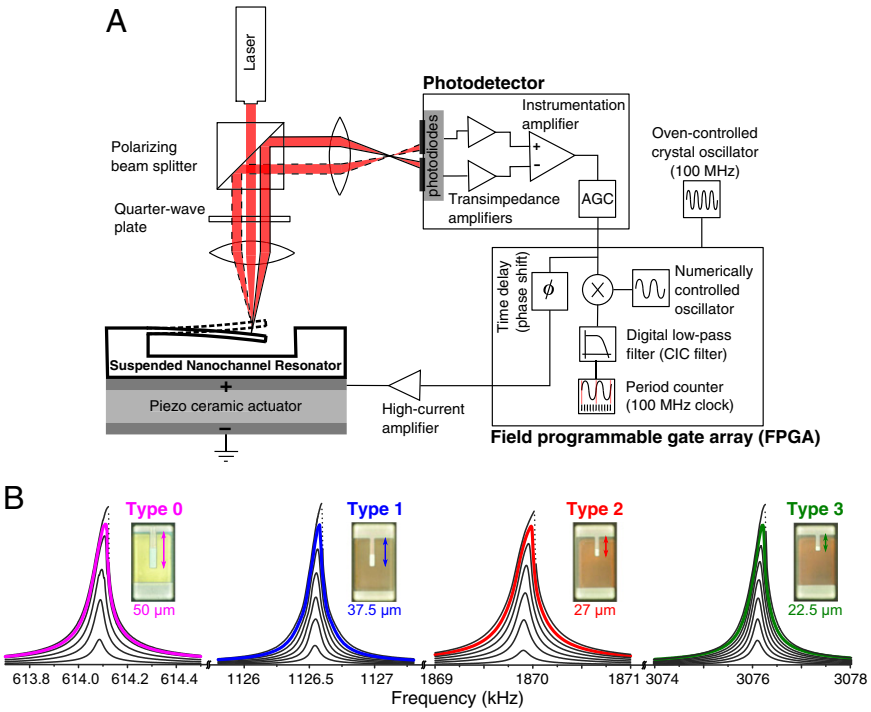

Fig. 1. Simplified schematic of the oscillator system with open-loop SNR frequency responses up to mechanical nonlinearity. (*A*) The SNR system (*SI Appendix*, Fig. S1) is a positive-feedback loop that keeps an SNR in oscillation. In the system, we used an optical lever to detect the cantilever deflection, a photodetector circuit to convert the laser deflection to a voltage signal, an FPGA to delay the photodetector signal and simultaneously measure the oscillation frequency, and an amplifier to drive the integrated piezoceramic actuator with the FPGA signal. The delay and the oscillation amplitude are controlled by the FPGA to achieve the minimum frequency noise. An oven-controlled crystal oscillator is used as the clock source for the FPGA. (*B*) Measured open-loop frequency responses of different types of SNRs used in this study (Table 1) for increasing drive levels, showing characteristic nonlinear behavior in the form of spring stiffening. The curves are normalized with respect to the peak amplitude at the onset of nonlinearity, which generates the minimum frequency noise in feedback. The frequency response curves at the onset of nonlinearity for each type are indicated as thicker, colored curves. (Insets) Optical micrographs of the cantilevers in the vacuum cavity with their lengths indicated below. Different types of cantilevers are color-coded, and the same color codes are used in Fig. 2.

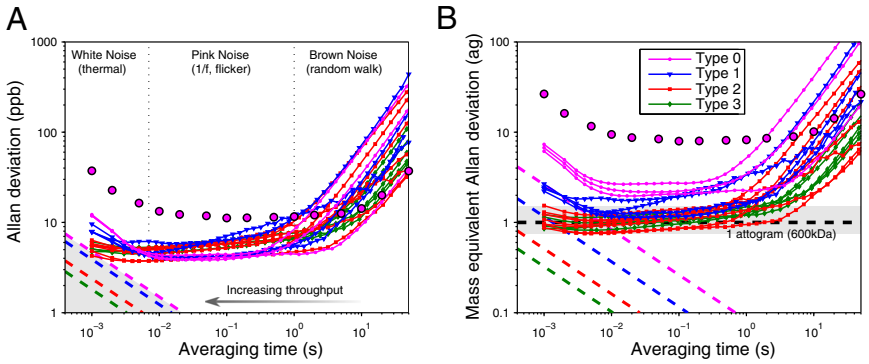

Fig. 2. Frequency noise and mass resolution of 20 different SNRs. (*A*) Frequency noise of each SNR, quantified as the Allan deviation and normalized by the mean frequency, is plotted as a function of averaging (gate) time. Ultimate noise limits imposed by thermal energy due to nonzero ambient temperature (*SI Appendix*, section 4) are shown as colored dashed lines in the lower left corner, and decrease as 1/(averaging time)$^{1/2}$. All lines are color-coded as in Fig. 1*B* with respect to the corresponding device types given in Table 1. Bigger pink circles show the Allan deviation of a type 0 cantilever as reported in ref. 17, which at 1-ms averaging time is more than 10× what we achieved in this work. The predominant noise mechanisms in the corresponding range of averaging times are indicated at the top and approximately delineated by thin dotted lines. (*B*) Mass resolution of each SNR, defined as the mass equivalent Allan deviation, is plotted as a function of the averaging time. Type 2 and 3 devices show typical mass resolutions of 0.75–1.5 ag (shaded region) from 1 to 200 ms averaging time. Colored dashed lines show the mass resolution limited by the thermal energy for corresponding type of cantilevers with matching color code. Measured mass sensitivities given in *SI Appendix*, Table S1 are used to convert the frequency noise in Fig. 2*A* to mass. For calculating the theoretical limits of mass resolution due to thermal energy, calculated mass sensitivities listed in Table 1 are used.

above the thermomechanical noise limits. For shorter (<10 to <1 ms) gate times, noise from the photodetector becomes the dominant factor (*SI Appendix*, Fig. S3), which sets a lower bound on the particle transit time and hence an upper bound on the throughput of the device. With further improvement of the detection system, it may be possible to achieve a 10-fold improvement in the throughput without sacrificing mass resolution (*SI Appendix*, section 3).

After we achieved mass sensitivities exceeding 16 mHz/ag and reduced frequency noise to 4 ppb, we focused on optimizing our peak detection scheme. We used the characteristic shape of a peak (30), determined by the flow path and the transit time of the particle, in a bank of matched filters for detecting the characteristic frequency modulation signal due to a particle transit with the maximum signal-to-noise ratio (31). The mass equivalent Allan deviation of type 2 and 3 devices is between 0.75 and 1.5 ag (gray region in Fig. 2*B*), which enables 3σ detection limits lower than 5 ag or 3 MDa (*SI Appendix*, Figs. S4 and S5).

Results

Mixture of Gold Nanoparticles. Mass distribution is an important measure of nanoparticle populations. We first demonstrated the mass resolution of our system by weighing a mixture of 10-, 15-, and 20-nm gold nanoparticles. Before analyzing the mixture, we calibrated the mass sensitivity (Hz/kg) of the resonator using size-calibrated gold nanoparticles (*SI Appendix*, Fig. S6). In a 97-min experiment, we measured more than 29,000 individual particles in the mixture (Fig. 3 *A* and *B*). The results show three distinct well-separated populations (Fig. 3*C*) ~9.1, 28.1, and 73.4 ag. Assuming all particles are spherical and uniformly dense, the mean sizes of the three populations are estimated to be 9.9, 14.4, and 19.7 nm, which agree well with the manufacturer specifications of 9.9, 14.3, and 20.4 nm (Fig. 3*D*). The coefficients of variation in diameter for each population were 7.4%, 5.3%, and 4.9%, respectively, compared with the datasheet values of <8% for 15- and 20-nm gold nanoparticles. Additionally, we compared our results to DLS measurements (*SI Appendix*, Table S2), which could not resolve the three populations separately in the gold nanoparticle mixture. We also tested the dynamic range of the SNRs by successfully weighing larger particles (150-, 200-, and 220-nm polystyrene beads) using the same operating, detection, and estimation conditions (*SI Appendix*, Fig. S7).

In addition to mass distribution, concentration is also a key parameter of nanoparticle suspensions. The SNR can provide a direct measure of nanoparticle concentration because the detection and estimation algorithm estimates the transit time of each particle (Fig. 3*B*) and the dimensions of the buried microfluidic channel are known. Based on the measurement shown in Fig. 3, the concentrations of 10-, 15-, and 20-nm gold nanoparticles in the mixture are 5.4×10^9, 3.6×10^9, and 3.7×10^9 particles per milliliter, respectively (see *SI Appendix*, section 9, for error analysis), which are comparable with the concentrations obtained from the particle datasheets (5.7×10^9, 3.1×10^9, and 3.9×10^9 particles per milliliter).

Heterogeneity of Exosomes from Different Cell Types. To demonstrate the capability of the SNRs to characterize relevant biological samples, we used exosomes, which are cell-derived vesicles present in the extracellular fluids that mediate intercellular communication via the exchange of proteins and genetic material (32, 33). Although there is immense scientific and clinical interest, detection and characterization of exosomes remain challenging. Purified exosomes from in vitro and clinical samples alike are heterogeneous because their size and density ranges from 30 to 100 nm and 1.13 to 1.19 g/cm^3, respectively (22), which translates into 2–100 ag buoyant mass in water. Moreover, exosomes from a mixed population of cells, i.e., normal vs. diseased cells, theoretically can differ in their cargo content, which in turn may alter their mass, size, and/or density. Optical methods such as DLS analysis can give comparative information about their mean size (*SI Appendix*, Table S3), but the heterogeneity and distribution shape of the populations, which may reflect differences in their biological functions, are difficult to measure. Therefore, we weighed exosomes that were produced by 3T3-J2 fibroblasts and primary hepatocytes, two inherently different cell types, which when cocultured have been shown to engage in both physical and molecular cell–cell interactions (34, 35). The buoyant mass distributions of exosomes derived from fibroblast and hepatocyte cells reveal clear differences in heterogeneity (Fig. 4). The relative broadness in buoyant mass of the fibroblast exosomes suggests the presence of either a larger or denser subpopulation compared with the exosomes derived

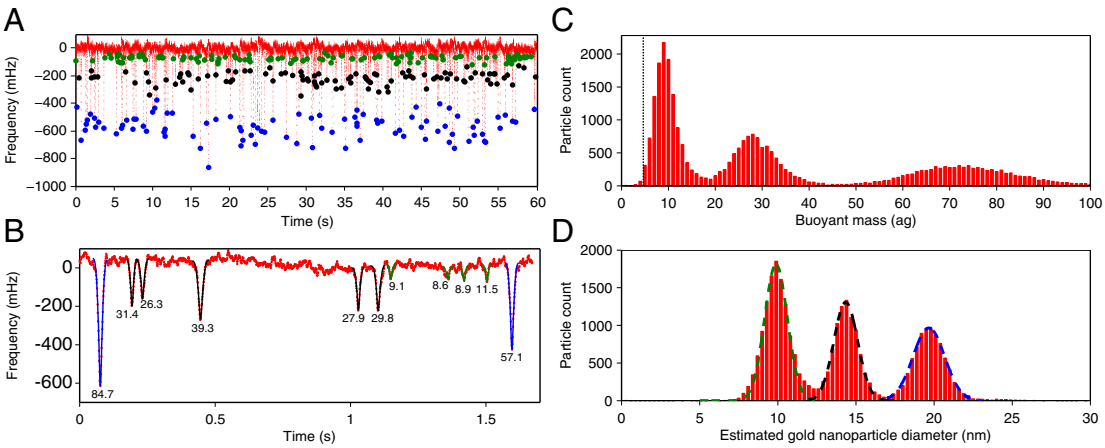

Fig. 3. Buoyant mass measurements of a mixture of 10-, 15-, and 20-nm gold nanoparticles. (*A*) An arbitrary 60-s oscillation frequency measurement around the resonant frequency of the SNR during a 97-min-long experiment. Data were acquired at 1 kHz and filtered with a five-point second-order Savitzky–Golay filter and a second-order IIR high-pass filter with 1-Hz cutoff frequency. Particles detected by the bank of matched filters (*Methods*) are marked with circles color-coded with respect to their buoyant masses (green for <18 ag, blue for >44 ag, black for in between). (*B*) Each detected peak is further analyzed for estimating the buoyant mass and the transit time of the particle by fitting it to the expected peak shape for a particle transiting the cantilever with a constant velocity. Estimated buoyant mass value for each detected particle is indicated underneath the peak along with the estimated color-coded peak shape. (*C*) Buoyant mass histogram of 29,000 particles detected during the experiment. The thin dotted line at ~5 ag is the limit of mass detection in the experiment. (*D*) Diameter histogram, calculated assuming particles are uniform spheres of density 19.3 g/cm^3. Dashed lines show fits to Gaussians. Particle peaks shown in *A* and *B* belong to the corresponding populations in *D* with the matching color. The fits indicate mean sizes of 9.9, 14.4, and 19.7 nm with coefficients of variation of 7.4%, 5.3%, and 4.9%, respectively.

from hepatocytes, which shows less dispersion with a 35% coefficient of variation in mass and a median of 8.6 ag; this translates into a median diameter of 48 nm (Fig. 4, *Inset*), assuming a spherical shape and uniform exosome density of 1.16 g/mL (see *SI Appendix*, Fig. S9 for the effect of density assumption on size). We observe a rapid increase in the exosome concentrations in both populations with decreasing buoyant mass from 20 to 10 ag. Similar size distributions have been measured using transmission electron microscopy (TEM) previously (36) on other types of exosome samples. It is worth noting that the shape of the distribution below ~7–8 ag is uncertain, because what we observe in this region is predominantly defined by the detection probability (*SI Appendix*, Fig. S8*C*). We repeated the experiments using a different cantilever on the same samples as well as on a second batch of purified fibroblast and hepatocyte exosomes. The results of the repeated runs (*SI Appendix*, Fig. S10) suggest the same difference in population heterogeneity presented in Fig. 4. We determined the concentrations of the purified stocks as being 3.3×10^{12} and 1.3×10^{12} particles per milliliter for fibroblast and hepatocyte exosomes, respectively, demonstrating that this technique can be used to quantify yields of exosome purifications as well.

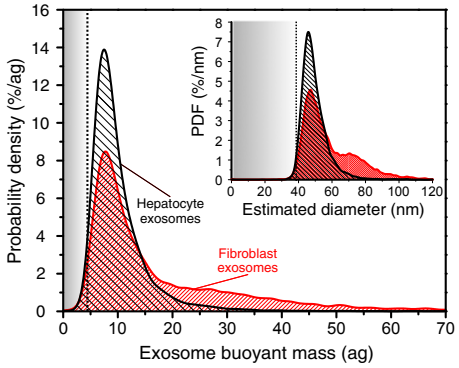

Fig. 4. Buoyant mass measurements of exosomes derived from different cell types. Buoyant mass distributions (kernel density estimates) of fibroblast-derived (red) and hepatocyte-derived (black) exosomal vesicles. Some 7,100 fibroblast exosomes and 9,600 hepatocyte exosomes are weighed using an SNR in 65-min and 76-min experiments, respectively. The limit of detection is depicted with a vertical dotted line close to 5 ag. (*Inset*) Estimation of exosome diameter by assuming a spherical shape and a constant exosome density of 1.16 g/mL throughout the populations. The vertical dashed line indicates the corresponding limit of mass detection as 39 nm.

Yield of DNA Origami–Gold Nanoparticle Assemblies. To further demonstrate the absolute concentration measurement capability of the SNR, we characterized the binding efficiency of functionalized gold nanoparticles to DNA origami structures. DNA nanotechnology has great promise for developing precise nanostructures, such as scaffolds for molecular nanodevices (37). However, practical and accurate methods are required for assessing the yield of complex DNA structures. We designed DNA origami structures as scaffolds with two and three binding sites for gold nanoparticles (*SI Appendix*, Figs. S11 and S12) and validated the binding of gold nanoparticles to DNA origami by gel electrophoresis and atomic force microscopy (AFM) (*SI Appendix*, Fig. S13). We weighed ssDNA-modified 15-nm gold nanoparticle binding agents with the SNR and observed that ~13% of the DNA-modified gold nanoparticle population were not singles (as defined as weighing more than 45 ag), with only 3.3% of the population being above 75 ag (9×10^7 particles per milliliter). This population results from two or more particles that agglomerated due to nonspecific binding of the modified DNA. We then weighed the DNA origami structures with two binding sites with modified gold nanoparticles. The abundance of the nonsingles increased to 32%, with 9% of this fraction weighing above 75 ag (1.3×10^8 particles per milliliter). This increase in the nonsingles indicates the successful binding of the gold nanoparticles to the DNA origami structure. Finally, we weighed the DNA origami structures with three binding sites with modified gold nanoparticles and, as expected, observed a broader distribution of particles compared with the previous samples. We calculated the concentration of the particles that are heavier than 75 ag

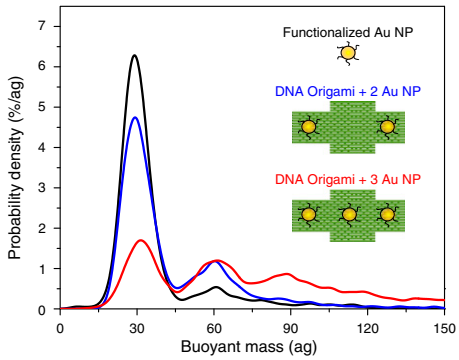

Fig. 5. Buoyant mass measurements of DNA origami–gold nanoparticle assemblies. Buoyant mass distributions (kernel density estimates) of functionalized 15-nm gold nanoparticles (Au NP) with ssDNA (black) mixed with DNA origami structures with two binding sites (blue) and DNA origami structures with three binding sites (red).

as 4.1×10^8 particles per milliliter, which constitute about 47% of the population. The resulting buoyant mass distributions for the three sample populations are shown in Fig. 5. Although gel electrophoresis can provide similar distributions, it cannot provide a measure of absolute concentration. Because the flow rate through the SNR in this experiment was ~3 nL/h, we envision that SNRs could ultimately be used as a real-time tool to quantify nanostructure assemblies.

Outlook

The demonstrations presented in this paper suggest that the SNR can be a valuable complement to the existing methods for characterizing nanoparticles in solution. High-precision mass measurement could allow us to identify signatures of pathology in blood plasma regardless of the molecular properties of the target. For example, glioblastoma cells are known to secrete microvesicles (50–500 nm) that have been implicated in angiogenesis (32). However, assessing if such nanoscale vesicles display a unique size or concentration signature has previously been extremely difficult. Combining volume measurements via resistive pulse sensing and buoyant mass measurements via the SNR at the level of individual nanoparticles would reveal their density, further increasing potential diagnostic power. For exosomes, measuring density would enable small particles with high amounts of cargo to be distinguished from large particles with limited cargo. Moreover, the SNR can potentially be used to discriminate between exosomes and larger extracellular microvesicles, which differ in size (38) and potentially differ in terms of their function. Because the contents of microvesicles and exosomes remain poorly characterized, multiparameter physical measurements together with molecular measurements could help elucidate their biological functions. In addition, future SNR implementations incorporating particle sorting and collection could allow purification and downstream analyses on a range of biological and synthetic nanoparticle populations. Such SNR implementations could be used for monitoring nanoparticle formation kinetics and ultimately for improving the techniques for engineering synthetic nanoparticles with desired properties.

Methods

SNR Fabrication. SNRs were manufactured by a previously described process (15, 17), which was performed at Innovative Micro Technology. The process enables each cantilever to freely oscillate in a dedicated vacuum cavity with an on-chip getter to maintain the high vacuum required for the high-Q operation. There are four fluidic ports drilled on the top glass wafer to access the two bypass channels (50 × 20 μm) separated 285 μm apart at each side of the cantilever. The U-shaped channel in the cantilever is connected to these bigger bypass channels by 140-μm channels with the same cross-section that is in the cantilever.

System Operation. The displacement noise of the cantilever due to the thermal energy is amplified in a positive feedback loop to achieve a sustainable self-oscillation according to the Barkhausen criteria (39) at the instantaneous resonant frequency of the cantilever. The frequency of oscillation is measured by period counting at 100 MHz using a digital heterodyne mixer and a low-pass filter coded in the FPGA (*SI Appendix*, section 2). We use computer-controlled electronic pressure regulators connected to pressurized glass sample vials to control the flow in the bypass channels and in the SNR.

Allan Deviation. The Allan deviation, $\sigma_A(\tau)$, of the oscillation frequency of an oscillator in a time period of τ is defined as in ref. 40:

$$\sigma_A(\tau) = \sqrt{\sigma_A^2(\tau)} \approx \sqrt{\frac{1}{2(N-1)} \sum_{k=2}^{N} \left(\frac{\bar{f}_k - \bar{f}_{k-1}}{f_0} \right)^2},$$

where $\bar{f}_k$ is the time average of the frequency measurement in the k^{th} time interval of τ within a total of N intervals, and f_0 is the mean oscillation frequency calculated over the entire duration of the noise measurement. In other words, the Allan deviation is calculated by averaging subsequent sections of the normalized frequency data of length τ, and then taking the difference between the means of contiguous segments.

Peak Detection and Estimation. Measured frequency data by the FPGA is sent to a control computer in real time via Ethernet and is recorded by the computer. The recorded data are analyzed afterward using postprocessing code in MatLab. First, the mean of the data are subtracted and the result is high-pass filtered by a second-order IIR notch filter with 1-Hz cutoff frequency. Next, the data are filtered with a bank of matched filters (*SI Appendix*, Fig. S4) with coefficients having a shape of a frequency peak (30) resulting from a particle passing through the SNR. The widths of the filters in the bank are adjusted to span the possible transit times of the particles for that particular experiment, and their amplitudes are normalized to their norms. At each point in time, the maximum among the matched filter outputs is selected and normalized to the corresponding filter norm to set the overall gain for a peak as unity. Finally, the peak positions in time that are above the limit of detection are determined (Fig. 3*A*), and the detected peaks are analyzed individually (Fig. 3*B*). The baseline and the peak shape are fit around each frequency minimum on the high-pass filtered frequency data using a least-squares fit algorithm.

Calibration. The mass sensitivity of a cantilever is determined by running a population of gold nanoparticles [RM 8012 by National Institute of Standards and Technology (NIST)] as a reference material before the actual experiment. Cantilever sensitivity is calculated using the mean particle diameter (26.5 nm), which was estimated by AFM, SEM, and TEM measurements as described in the reference material datasheet. The resulting mass histogram and size estimation are given in *SI Appendix*, Fig. S6.

Gold Nanoparticle Measurements. A type 2 device (11M in *SI Appendix*, Table S1) was used to weigh the nanoparticle mixture comprised of 10- (NIST RM 8011), 15-, and 20-nm (EMGC15 and EMGC20 from BBI Solutions) gold. Samples were diluted in filtered (0.22 μm) deionized water 300, 150, and 60 times, respectively. We mixed 0.5 mL of diluted 10-, 15-, and 20-nm gold particles together before the experiment, which increased the total dilutions to 900, 450, and 180 times, respectively. The accuracy of the concentration estimation increases with the signal-to-noise ratio of the particles in the sample (*SI Appendix*, section 9). Therefore, we calculated flow rate in the SNR using the 20-nm particle signal, which has the highest signal-to-noise ratio in the mixture.

Functionalization of Gold Nanoparticles with DNA. DNA-modified gold nanoparticles (*SI Appendix*, Fig. S11) were prepared using previous reports (41). Gold nanoparticles (15 nm; Ted Pella Inc.) were stabilized with Bis(*p*-sulfonatophenyl)phenylphosphine dihydrate dipotassium salt (BSPP). BSPP (18 mg) was dissolved in gold nanoparticle solution (25 mL), and the mixture was stirred overnight at room temperature. Sodium chloride was added slowly to the solution with stirring until the color changed from red to light purple. The resulting solution was centrifuged at 966 × *g* for 30 min. The supernatant was carefully removed and the gold nanoparticles were dispersed in 0.5 mL BSPP (2.5 mM) with 0.5 mL methanol. The solution was centrifuged at 21,130 × *g* for 30 min. The supernatant was removed and gold nanoparticles

were dispersed again in 0.25 mL BSPP (2.5 mM). Next, 80 μL T_{28}-SH DNA (100 μM) was activated with 20 μL Tris-(2-carboxyethyl)phosphine hydrochloride (100 mM). The activated thiol-modified DNA was purified using a NAP-5 column (GE Healthcare). The phosphinated gold nanoparticles and thiol-modified DNA (gold nanoparticle:DNA = 1:200) were incubated in 1 M Tris, 0.9 M boric acid, 0.01 M EDTA (pH 8.0) containing NaCl (50 mM) for 15 h at room temperature, which enabled the stabilization of gold nanoparticles under high-salt conditions.

Preparation of the DNA Origami. The molar ratio of 1:5 between M13mp18 viral ssDNA and staple strands was used. DNA origami was assembled in 40 mM Tris, 20 mM acetic acid, 2 mM EDTA (pH 8.0) buffer (1×) containing magnesium acetate (12.5 mM) by annealing from 95 °C for 5 min to 60 °C over 35 min, and cooled further to 15 °C over 135 min. The annealing product was purified using spin filtration (MWCO, 100 K; Millipore) to remove extra staple strands. The constructed DNA origami was examined by AFM (*SI Appendix*, Fig. S12). DNA origami structures with two and three binding sites were prepared by substituting original staple strands for hook staple strands. Purified DNA origami was mixed with thiol-modified gold nanoparticles and annealed from 37 °C to 15 °C over 110 min. Finally, we examined the products purified by agarose gel by AFM (*SI Appendix*, Fig. S13).

Exosome Experiments. Exosomes were purified from supernatants of 3T3-J2 fibroblasts cultured at 37 °C, 5% CO_2 in DMEM with high glucose, 10% (vol/vol) exosome-depleted FBS, and 1% penicillin–streptomycin. 3T3-J2 fibroblasts were cultured until ∼60% confluency at which point media was replaced with exosome-depleted fibroblast media. After 48 h, 3T3-J2 media was collected and centrifuged at 1,800 × *g* for 10 min to remove cells. Hepatocytes exosomes were obtained from primary rat hepatocytes cultured in DMEM with high glucose, 10% (vol/vol) exosome-depleted FBS, 0.5 U/mL insulin, 7 ng/mL glucagon, 7.5 μg/mL hydrocortisone, and 1% penicillin–streptomycin. Twelve million hepatocytes were seeded in T150 flasks for 3 h to obtain ∼80% confluency. After 3 h, media was collected, centrifuged at 3,000 rpm for 10 min to remove cells, and replaced with fresh exosome-depleted hepatocyte media. Following an additional 24 h of culture, hepatocyte media was again collected, centrifuged at 3,000 rpm for 10 min to remove cells, and pooled with hepatocyte media collected the previous day. Exosomes were purified from media using differential centrifugation. Briefly, media was centrifuged at 10,000 × *g* for 1 h and subsequently processed through a 0.22-μm filter. A crude exosome pellet was obtained by ultracentrifugation at 100,000 × *g* for 3 h at 4 °C and resuspended in 0.22 μm filtered PBS. Washed exosomes were again pelleted at 100,000 × *g* for 2 h at 4 °C and resuspended in 150 μL filtered PBS. To remove any copurified protein complexes, exosomes were further purified by size-exclusion chromatography over a Sepharose CL-4B resin column (GE Healthcare). Exosome containing fractions, as detected by DLS analysis, were pooled and pelleted at 100,000 × *g* for 2 h at 4 °C. Finally, purified exosomes were resuspended in 100 μL filtered PBS for further analysis. We diluted the prepared fibroblast exosomes 500× and hepatocyte exosomes 200× in 0.22 μm filtered 1× PBS before running the populations through a type 3 SNR (see 7B in *SI Appendix*, Table S1).

ACKNOWLEDGMENTS. We thank the Koch Institute Swanson Biotechnology Center for technical support. Support for this work was provided by Institute for Collaborative Biotechnologies Contract W911NF-09-D-0001 from the US Army Research Office Center for Integration of Medicine and Innovative Technology Contract 09-440; National Science Foundation Grant 1129359; and Koch Institute Support (core) Grant P30-CA14051 from the National Cancer Institute. S.N.B. is a Howard Hughes Medical Institute Investigator.

1. Peer D, et al. (2007) Nanocarriers as an emerging platform for cancer therapy. *Nat Nanotechnol* 2(12):751–760.
2. Morachis JM, Mahmoud EA, Almutairi A (2012) Physical and chemical strategies for therapeutic delivery by using polymeric nanoparticles. *Pharmacol Rev* 64(3):505–519.
3. Chi EY, Krishnan S, Randolph TW, Carpenter JF (2003) Physical stability of proteins in aqueous solution: Mechanism and driving forces in nonnative protein aggregation. *Pharm Res* 20(9):1325–1336.
4. Sauerborn M, Brinks V, Jiskoot W, Schellekens H (2010) Immunological mechanism underlying the immune response to recombinant human protein therapeutics. *Trends Pharmacol Sci* 31(2):53–59.
5. Théry C, Ostrowski M, Segura E (2009) Membrane vesicles as conveyors of immune responses. *Nat Rev Immunol* 9(8):581–593.
6. Anderson W, Kozak D, Coleman VA, Jämting ÅK, Trau M (2013) A comparative study of submicron particle sizing platforms: Accuracy, precision and resolution analysis of polydisperse particle size distributions. *J Colloid Interface Sci* 405:322–330.
7. Lange H (1995) Comparative test of methods to determine particle size and particle size distribution in the submicron range. *Part Part Syst Charact* 12(3):148–157.
8. Mahl D, Diendorf J, Meyer-Zaika W, Epple M (2011) Possibilities and limitations of different analytical methods for the size determination of a bimodal dispersion of metallic nanoparticles. *Colloids Surf Physicochem Eng Asp* 377(1-3):386–392.
9. Fraikin J-L, Teesalu T, McKenney CM, Ruoslahti E, Cleland AN (2011) A high-throughput label-free nanoparticle analyser. *Nat Nanotechnol* 6(5):308–313.
10. Roberts GS, et al. (2010) Tunable nano/micropores for particle detection and discrimination: Scanning ion occlusion spectroscopy. *Small* 6(23):2653–2658.
11. Chaste J, et al. (2012) A nanomechanical mass sensor with yoctogram resolution. *Nat Nanotechnol* 7(5):301–304.
12. Jensen K, Kim K, Zettl A (2008) An atomic-resolution nanomechanical mass sensor. *Nat Nanotechnol* 3(9):533–537.
13. Naik AK, Hanay MS, Hiebert WK, Feng XL, Roukes ML (2009) Towards single-molecule nanomechanical mass spectrometry. *Nat Nanotechnol* 4(7):445–450.
14. Hanay MS, et al. (2012) Single-protein nanomechanical mass spectrometry in real time. *Nat Nanotechnol* 7(9):602–608.
15. Burg TP, et al. (2007) Weighing of biomolecules, single cells and single nanoparticles in fluid. *Nature* 446(7139):1066–1069.
16. Barton RA, et al. (2010) Fabrication of a nanomechanical mass sensor containing a nanofluidic channel. *Nano Lett* 10(6):2058–2063.
17. Lee J, Shen W, Payer K, Burg TP, Manalis SR (2010) Toward attogram mass measurements in solution with suspended nanochannel resonators. *Nano Lett* 10(7):2537–2542.
18. Yang YT, Callegari C, Feng XL, Ekinci KL, Roukes ML (2006) Zeptogram-scale nanomechanical mass sensing. *Nano Lett* 6(4):583–586.
19. Ekinci KL, Roukes ML (2005) Electromechanical transducers at the nanoscale: Actuation and sensing of motion in nanoelectromechanical systems (NEMS). *Small* 1(8-9):786–797.
20. Feng XL, White CJ, Hajimiri A, Roukes ML (2008) A self-sustaining ultrahigh-frequency nanoelectromechanical oscillator. *Nat Nanotechnol* 3(6):342–346.
21. Arlett JL, Roukes ML (2010) Ultimate and practical limits of fluid-based mass detection with suspended microchannel resonators. *J Appl Phys* 108(8):084701.
22. Théry C, Zitvogel L, Amigorena S (2002) Exosomes: Composition, biogenesis and function. *Nat Rev Immunol* 2(8):569–579.
23. Ekinci KL, Yang YT, Roukes ML (2004) Ultimate limits to inertial mass sensing based upon nanoelectromechanical systems. *J Appl Phys* 95(5):2682–2689.
24. Greywall DS, Yurke B, Busch PA, Pargellis AN, Willett RL (1994) Evading amplifier noise in nonlinear oscillators. *Phys Rev Lett* 72(19):2992–2995.
25. Rutman J, Walls FL (1991) Characterization of frequency stability in precision frequency sources. *Proc IEEE* 79(6):952–960.
26. Leeson D (1966) A simple model of feedback oscillator noise spectrum. *Proc IEEE* 54(2):329–330.
27. Rubiola E (2009) *Phase Noise and Frequency Stability in Oscillators* (Cambridge Univ Press, Cambridge, UK).
28. Albrecht TR, Grütter P, Horne D, Rugar D (1991) Frequency modulation detection using high-Q cantilevers for enhanced force microscope sensitivity. *J Appl Phys* 69(2):668–673.
29. Cleland AN, Roukes ML (2002) Noise processes in nanomechanical resonators. *J Appl Phys* 92(5):2758–2769.
30. Dohn S, Svendsen W, Boisen A, Hansen O (2007) Mass and position determination of attached particles on cantilever based mass sensors. *Rev Sci Instrum* 78(10):103303–103333.
31. Hippenstiel RD (2002) *Detection Theory: Applications and Digital Signal Processing* (CRC, Boca Raton, FL).
32. Skog J, et al. (2008) Glioblastoma microvesicles transport RNA and proteins that promote tumour growth and provide diagnostic biomarkers. *Nat Cell Biol* 10(12):1470–1476.
33. Peinado H, et al. (2012) Melanoma exosomes educate bone marrow progenitor cells toward a pro-metastatic phenotype through MET. *Nat Med* 18(6):883–891.
34. Hui EE, Bhatia SN (2007) Micromechanical control of cell-cell interactions. *Proc Natl Acad Sci USA* 104(14):5722–5726.
35. Khetani SR, Bhatia SN (2008) Microscale culture of human liver cells for drug development. *Nat Biotechnol* 26(1):120–126.
36. van der Pol E, et al. (2010) Optical and non-optical methods for detection and characterization of microparticles and exosomes. *J Thromb Haemost* 8(12):2596–2607.
37. Douglas SM, Bachelet I, Church GM (2012) A logic-gated nanorobot for targeted transport of molecular payloads. *Science* 335(6070):831–834.
38. Simons M, Raposo G (2009) Exosomes—vesicular carriers for intercellular communication. *Curr Opin Cell Biol* 21(4):575–581.
39. Hajimiri A, Lee TH (1999) *The Design of Low Noise Oscillators* (Kluwer Academic, Boston).
40. Barnes J, et al. (1971) Characterization of frequency stability. *IEEE Trans Instrum Meas* 20(2):105–120.
41. Sharma J, et al. (2008) Toward reliable gold nanoparticle patterning on self-assembled DNA nanoscaffold. *J Am Chem Soc* 130(25):7820–7821.

Supporting Information for
Weighing nanoparticles in solution at the attogram scale

Selim Olcum[a,b,1], Nathan Cermak[c,1], Steven C. Wasserman[a], Kathleen S. Christine[d,e], Hiroshi Atsumi[f], Kristofor Payer[g], Wenjiang Shen[h], Jungchul Lee[i], Angela M. Belcher[a,b,f], Sangeeta N. Bhatia[b,d,e,j,k], Scott R. Manalis[a,b,c,l,2]

[a]Department of Biological Engineering, Massachusetts Institute of Technology, Cambridge, MA, 02139, USA
[b]Koch Institute for Integrative Cancer Research, Massachusetts Institute of Technology, Cambridge, MA, 02139, USA.
[c]Computational and Systems Biology Initiative, Massachusetts Institute of Technology, Cambridge, MA, 02139, USA
[d]Harvard-MIT Health Sciences and Technology, Institute for Medical Engineering and Science, Massachusetts Institute of Technology, Cambridge, MA, 02139, USA
[e]Institute for Medical Engineering and Science, Massachusetts Institute of Technology, Cambridge, MA, 02139, USA
[f]Department of Materials Science and Engineering, Massachusetts Institute of Technology, Cambridge, MA, 02139, USA
[g]Microsystems Technology Laboratories, Massachusetts Institute of Technology, Cambridge, MA, 02139 USA
[h]Innovative Micro Technology, Santa Barbara, CA, 93117
[i]Department of Mechanical Engineering, Sogang University, Seoul 121-742, Republic of Korea
[j]Department of Electrical Engineering and Computer Science, Massachusetts Institute of Technology, Cambridge, MA, 02139, USA
[k]Howard Hughes Medical Institute, Cambridge, Massachusetts 02139, USA
[l]Department of Mechanical Engineering, Massachusetts Institute of Technology, Cambridge, MA, 02139, USA

[1] These authors contributed equally to this work.

Table of Contents

1 Device parameters

Type	Device ID	Frequency (kHz)	Q factor	$\delta f/\delta m$ (mHz/ag)
0	S1	517	22,000	0.95
0	S3	545	14,000	0.95
0	S4	590	17,000	0.99
0	S6	577	24,000	1.08
1	4I	1205	9,000	4
1	5B	1240	12,000	4.9
1	8O	973	9,500	3.4
1	X4	1127	20,000	4
2	X6	2493	20,000	14.3
2	13L	1871	15,000	9.3
2	4K	2201	16,000	9.1
2	11M	1918	11,000	8.4
2	5J	2214	18,000	10.5
2	5M	2125	16,000	10.9
2	7A	2873	15,000	14
3	8N	2887	17,500	16
3	13M	2662	15,000	14.2
3	4J	3266	16,000	18
3	5N	2079	17,000	14
3	7B	3910	15,000	21.4

Table S1 Measured parameters of the cantilevers used in this study. The resonant frequencies and quality factors of the SNRs used in Figure 2 are measured by a lock-in amplifier (SRS-SR844) when the cantilevers are filled with ultra-pure deionized water. We measured the mass sensitivity of the cantilevers by weighing size-calibrated NIST traceable particles in each cantilever i.e. 30 nm gold (NIST SRM8012), 150 nm (Thermo Scientific 3150A), 200 nm (Thermo Scientific 3200A) and 220 nm (Thermo Scientific 3220A) polystyrene.

2 System operation

The cantilevers used in this work are operated in self-oscillation mode in a positive feedback loop. The image of the oscillator system is given in Fig. S1. The motion of the cantilever is converted to the deflection of a laser beam bounced off of the tip using an optical lever setup (Fig. 1a). We used an ultra-low noise diode lab laser module (Coherent 635 nm, 5 mW) as the laser source. We cleaned up and expanded the laser source by a spatial filter (0.5NA 13.86 mm aspherical lens, 20 μm pinhole) and a collimating spherical lens (f=30 mm) to achieve a coherent ~3 mm-diameter filtered laser beam. Additionally, we used a film polarizer to tune the incident laser power on the cantilever. Increasing the laser power causes the temperature of the cantilever to fluctuate, which can be observed as frequency fluctuations of the oscillator. This is particularly the case for smaller cantilevers (Type 2 and 3). In all cases, we used the maximum laser power that can give the minimum frequency noise. The laser beam is focused on the cantilever tip using a 20X objective (Nikon LU Plan ELWD 0.4NA). The reflected laser beam is focused on the photodetector by an achromatic doublet lens (Thorlabs AC254-30-A). The spot size on the photodetector is adjusted by changing the distance of the focusing lens to the photodetector.

We used a custom-made low-noise photodetector circuit to transform the angular deflection acquired from the optical lever setup to an electrical signal by a high-speed split PIN photo-diode (Hamamatsu S4204). We used ultra-low-noise transimpedance amplifiers (OPA847) with 5 MHz 3 dB-bandwidth followed by a high speed instrumentation amplifier (AD8130) to convert the differential optical deflection signal on the split photodiode to a voltage signal. The generated voltage signal is amplified by an automatic gain control (AGC) stage to achieve constant amplitude at the output of the photodetector. The output amplitude can be tuned by a DC input voltage connected to the AGC stage.

The optimal delay required in the loop for stable self-oscillation is introduced by a field programmable gate array (FPGA, Altera Cyclone IV on DE2-115). The analog signal in the loop is interfaced with the digital signal in the FPGA using the Terasic AD/DA conversion board at 100 MSPS with 14-bit convertors. The FPGA and the conversion board run on an external 100 MHz oven controlled crystal oscillator clock (Abracon AOCJY2-E-H1C). The delay algorithm in the FPGA is capable of achieving sub-clock delays (39 ps minimum) using numerical interpolation, which converts to less than 0.1 degree resolution for adjusting the phase shift of

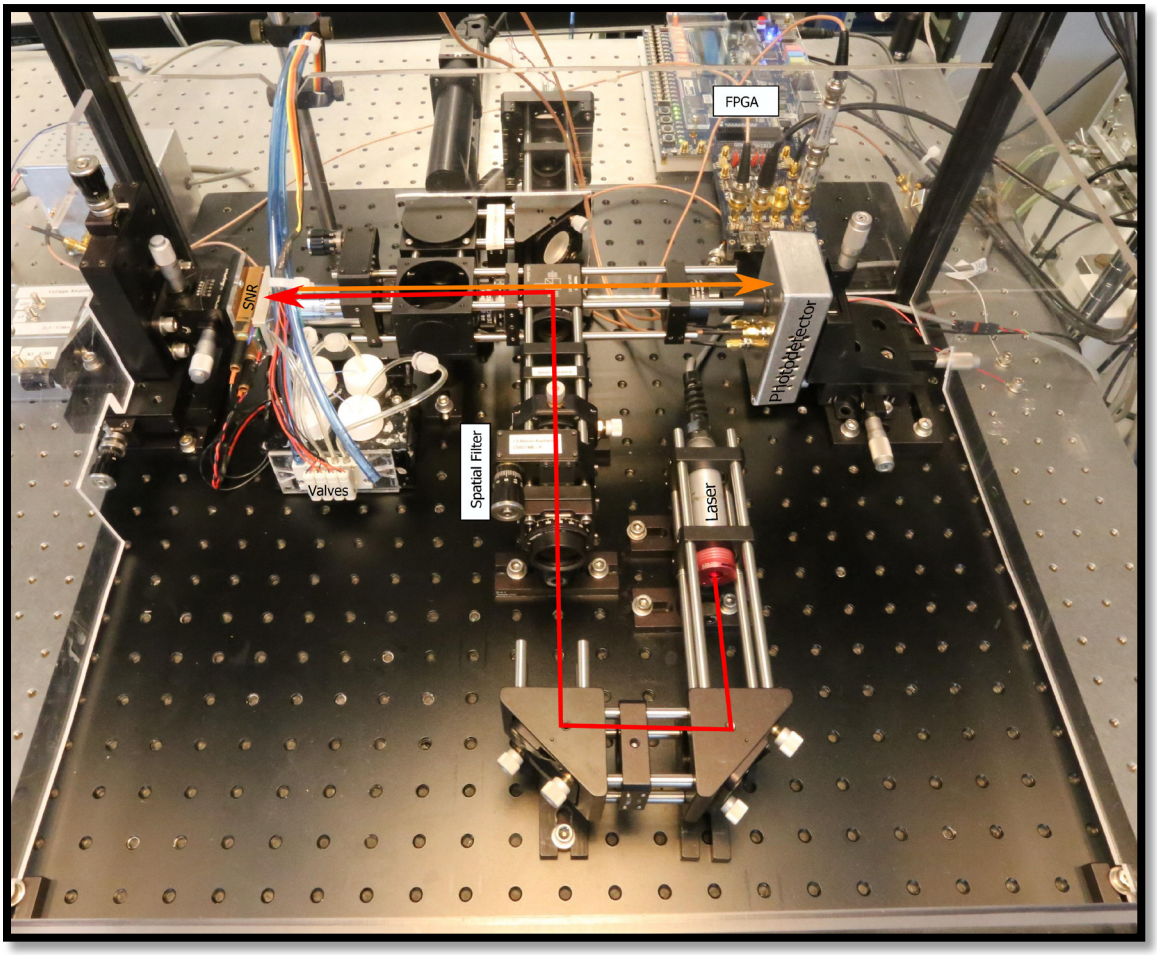

Figure S1 Photograph of the oscillator system. The incident laser path onto the cantilever is indicated with a red line. The orange line shows the reflected laser path from the cantilever.

the highest frequency oscillators used in this work (4 MHz).

Since the amplitude of photodetector output is kept constant by the AGC, the oscillation amplitude of a cantilever can be adjusted by the FPGA independently. The output of the FPGA is amplified with a gain of 15 dB using an amplifier utilizing a high current OPAMP (LT1210) output stage, which drives a piezoceramic actuator (American Piezo Co. APC841, 7x7x0.2 mm) integrated underneath the SNR chip.

The frequency of oscillation is measured by period counting at 100 MHz using a digital heterodyne mixer and a low-pass filter coded in the FPGA. The signal is mixed with a reference sinusoid generated by a numerically-controlled oscillator (NCO). The heterodyned signal is then filtered using a 3-stage cascaded integrator comb (CIC) filter with a width of 500 data points (5 µs) and then up-sampled (1st-order hold) back to 100 MHz. The number of clock cycles in between zero crossings of the resulting signal is counted to infer the period. Note that the difference of the reference frequency and the oscillation frequency determines the RF measurement bandwidth.

The FPGA communicates with a control computer via Ethernet. The computer is used to control the delay in the loop and the amplitude of oscillation as well as the bandwidth of the frequency measurement algorithm. Measured oscillation frequency waveform (baseband signal) is recorded by the control computer for post-processing.

3 Detector noise

For performing an analysis on the noise sources limiting the noise performance of the SNRs, we first measured the voltage noise power spectrum density of the photodetector output, S_V^{pd}(V^2/Hz) in our optical lever setup using a spectrum analyzer (HP 4395A) when the water-filled cantilevers were driven only by the thermal energy due to the non-zero ambient temperature, T (~300K). The displacement noise spectral density of a cantilever due to thermal energy, S_x^{th} (m^2/Hz) as a function of frequency, ω is given by(1):

$$S_x^{th}(\omega) = \frac{4\omega_0^3 k_B T}{kQ} \frac{1}{(\omega_0^2 - \omega^2)^2 + (\omega\omega_0/Q)^2} \quad (1)$$

where, k_B, k, Q and ω_0 are Boltzmann constant and stiffness, quality factor and resonant frequency of the cantilever. At the resonant frequency, above equation reduces to $4k_BTQ/\omega_0 k$, which can be used to calculate the responsivity (V/m) of the optical lever setup as follows:

$$R = \sqrt{\frac{S_V^{pd}(\omega_0) - S_V^{pd}(\omega \neq \omega_0)}{S_x^{th}(\omega_0)}} = \sqrt{\frac{S_V^{pd}(\omega_0) - S_V^{pd}(\omega \neq \omega_0)}{4k_BTQ/\omega_0 k}} \quad (2)$$

For calculating the responsivity of the optical lever setup we used the measured parameters of the cantilever under test. The resonant frequencies and the quality factors are given in Table S1. The stiffness of a cantilever is calculated using the measured mass sensitivity values in the same table using the following relation:

$$\frac{\delta f}{\delta m} = -\frac{f_0}{2m^*} = -\frac{2\pi^2 f_0^3}{k} \quad (3)$$

where m^* is the effective mass of the cantilever. Using the above relations and measured cantilever parameters, we calculated the displacement noise power spectral density for different types of SNRs used in this work. The results are given in Figure S2**.** The red circles are

the spectrum analyzer (HP 4395A) measurements referred to displacement domain performed at 3 Hz resolution bandwidth with 100 averages. The dashed black curves are calculated using equation (1) and the dashed green lines are the calculated noise density of the photodetector referred to the displacement domain. We measured the photodetector noise floor between 90-140 $fm/\sqrt{Hz}$ for all types of cantilevers. The noise of the optical lever setup is limited by the thermomechanical vibrations of the cantilevers at the vicinity of their resonant frequencies and by the photodetector noise floor at frequencies away from the resonant frequency.

For investigating the effect of the displacement noise on the oscillator performance we measured the root-mean-square (RMS) frequency noise of the cantilevers when they were oscillating in feedback. We then compared the acquired noise measurements to the RMS frequency noise due to thermal energy and detector noise, which can be calculated following the analysis given by Albrecht et al.(1) as:

$$\langle \delta\omega^2 \rangle = \frac{k_B T}{k\langle x_c^2 \rangle}\frac{\omega_0 B}{Q} + \frac{B^3 S_x^{pd}}{12\,\langle x_c^2 \rangle} \qquad (4)$$

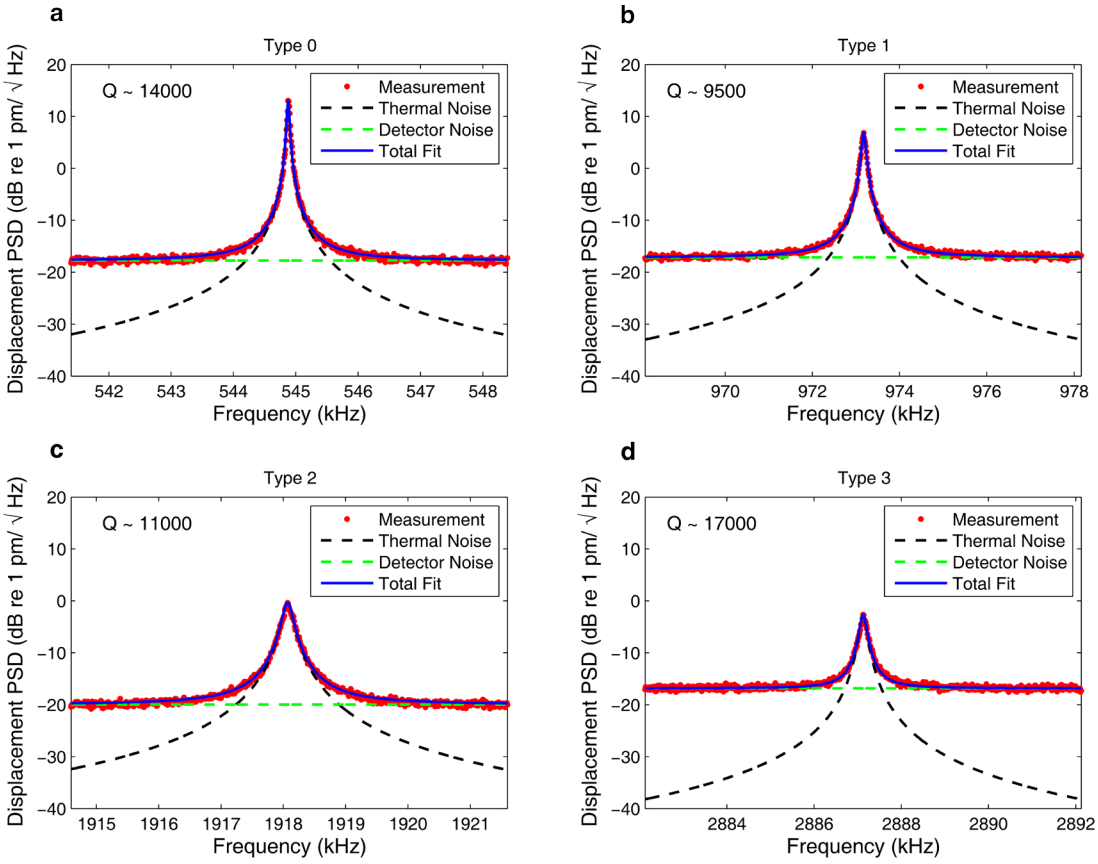

Figure S2 Displacement noise density of SNRs of different types. The red circles are calculated by referring the measured voltage power spectral density of the cantilevers due to thermal vibrations to displacement domain. The dashed black lines are the calculated displacement noise density of the cantilevers due to thermal vibrations using equation (1). The green dashed lines are the calculated displacement noise floor of the photodetector. The spectrum measurements are performed using 3 Hz resolution bandwidth and 100 averages.

where B is the RF measurement bandwidth, S_x^{pd} is the photodetector power spectral density referred to the displacement domain in m^2/Hz and $\langle x_c \rangle$ is the RMS displacement of the cantilever tip. The first term in this equation is due to the thermal energy and the second term is due to the photodetector noise. The RMS displacements of the cantilevers used in this work are limited by the mechanical nonlinearity. We used the approximate displacement expression given by Arlett et al.(2) converted to RMS at the onset of nonlinearity as

$$\langle x_c \rangle = 5.46 \frac{L}{\sqrt{2Q}} \qquad (5)$$

where L is the length of the cantilever. The calculated RMS noise values as a function of measurement bandwidth are given in Figure S3. The red dots are the measured RMS frequency noise in 1 second intervals as a function of measurement bandwidth and when the cantilevers are in self-oscillation at their onset of nonlinearity. The dashed black lines are the estimated noise due to the thermal energy and the black solid curves are the estimated noise due to the combination of thermal energy and the photodetector noise as given in equation (4).

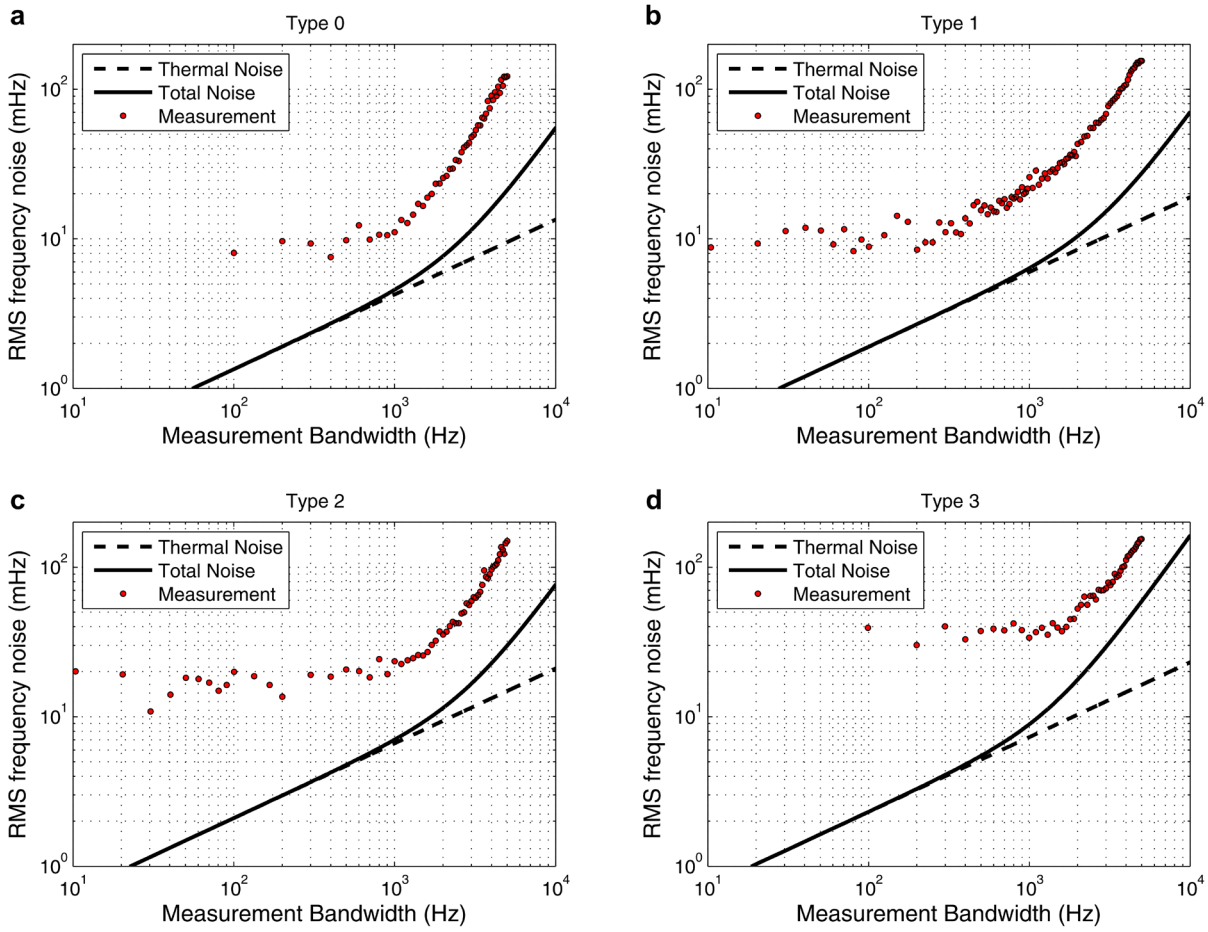

Figure S3 Root-mean-square frequency noise of the oscillators are measured as a function of measurement bandwidth for different types of SNRs and plotted as red circles. The dashed black lines are the RMS frequency noise due to thermal energy calculated using the first term in equation (4). The solid black lines are the calculated RMS noise due to the detector noise floor and thermal energy. Each red circle is calculated using 1 second of frequency noise measurement.

From Figure S3, we can see that all types of cantilevers are limited by the photodetector noise at wide measurement bandwidths. Increased noise at wide measurement bandwidth limits the throughput for better mass resolution cases. Approximately flat RMS frequency noise at narrower bandwidth operation is also observed in Allan deviation curves in Fig. 2 as the flicker noise region. Especially for device types 2 and 3, if the displacement noise floor of the motion detector can be reduced, the throughput of the device can be increased up to 10-fold without sacrificing mass resolution.

4 Thermal noise limit on Allan deviation

In order to calculate the fundamental noise limit on frequency stability in terms of Allan deviation due to the thermal noise on the cantilever, we treat the cantilever as a damped harmonic oscillator. The spectral density of the random displacements of the cantilever, $S_x^{th}(\omega)$ was given in equation (1), which is used here to calculate the spectral density of the phase fluctuations, $S_\varphi^{th}(\omega)$:

$$S_\varphi^{th}(\omega) = \frac{S_x^{th}(\omega)}{\langle x_c \rangle^2} = \frac{4\omega_0^3 k_B T}{k\langle x_c \rangle^2 Q} \frac{1}{(\omega_0^2 - \omega^2)^2 + (\omega\omega_0/Q)^2} \quad (6)$$

Equation (6) can be approximated as follows (1) for very high Q oscillators:

$$S_\varphi^{th}(\omega) \approx \frac{\omega_0 k_B T}{k\langle x_c \rangle^2 Q} \frac{1}{(\omega - \omega_0)^2} \quad (7)$$

If we convert the above relation to baseband around the carrier frequency ω_0 by defining a modulation frequency $\omega_m = \omega - \omega_0$, we get the phase noise density as:

$$S_\varphi^{th}(\omega_m) \approx \frac{\omega_0 k_B T}{k\langle x_c \rangle^2 Q} \frac{1}{\omega_m^2} = \frac{\omega_0 k_B T}{E_C Q} \frac{1}{\omega_m^2} \quad (8)$$

where E_C is the carrier energy defined as $k\langle x_c \rangle^2$. The Allan variance due to the phase noise density of an oscillator is calculated using the following relation (3):

$$\sigma_A^2(\tau) = 2\left(\frac{2}{\omega_0 \tau}\right)^2 \int_0^\infty S_\varphi(\omega)\, sin^4(\omega\tau/2)\, d\omega \quad (9)$$

If we evaluate the integral above using the phase noise density in equation (8), we get:

$$\sigma_A^{th}(\tau) = \sqrt{\frac{\pi k_B T}{\tau\, E_C\, Q\, \omega_0}} = \sqrt{\frac{k_B T}{2\,\tau\, E_C\, Q\, f_0}} \quad (10)$$

Since the cantilevers in this work are driven at their onsets of nonlinearity, we use the approximate expression given in equation (5) as the RMS displacement to calculate the nonlinearity limited Allan deviation due to thermal noise,

$$\sigma_{A,non}^{th}(\tau) = \frac{1}{5.46L} \sqrt{\frac{k_B T}{\tau\, k\, f_0}} \quad (11)$$

which is independent of the quality factor. Therefore, as long as an oscillator is driven at its onset of nonlinearity, the lowest Allan deviation that can be achieved does not depend on the quality factor of the resonator. In that case the practically achievable stability would be limited by the coupling efficiency of the actuator or the power handling capability of the resonator. The fundamental limits on the Allan deviation of the oscillators used in this work, which are plotted

in Figure 2 of the manuscript as a function of gate time, τ, are calculated using equation (11) and the design parameters given in Table 1 of the manuscript.

5 Limit of detection

We calculated limits of mass detection of the SNRs by taking measurements of instrument noise (the same data as used for Fig. 2), filtering with an FIR filter, h_T, and calculating the standard deviation, σ_T of the remaining signal, illustrated in Figure S4. The filter h_T was defined as the peak shape given in Dohn et al.(4) for a peak of width T, with the mean subtracted and then the amplitude normalized such that the gain for a peak of the same width was unity. This approach deviates slightly from the truly optimal (in terms of signal-to-noise ratio) FIR filter for detecting a signal s, which is given by

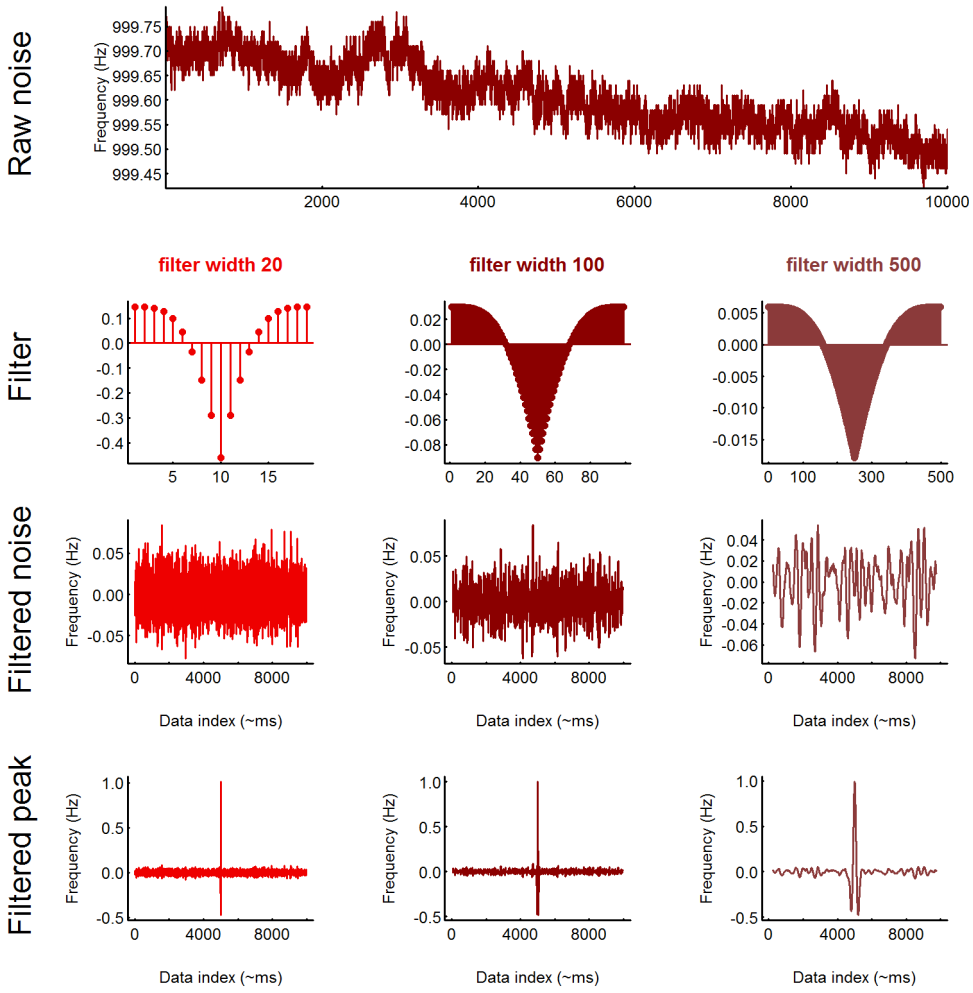

Figure S4 Illustration of the method used for calculating limits of detection using matched filters of varying peak widths. Raw noise is filtered with a filter shaped like the signal generated by a particle transiting the cantilever, with the mean subtracted. The filters are normalized such that a 1 Hz peak input yields a 1 Hz peak out.

$$h = \alpha R^{-1} s \quad (12)$$

where h is the vector of filter coefficients (taps), α is a normalization constant, and R is the covariance matrix of the noise. Because our noise has long correlation times (a defining characteristic of 1/f and $1/f^2$ noise) leading to extremely long optimal FIR filters, instead of multiplying our signal by R^{-1}, we approximate the true matched filter by simply subtracting off the mean (DC component) of our peak shape (shown in second row of Figure S4). This effectively includes a high-pass component in our filter that should reject frequencies below those in our peak. After filtering, we calculate the standard deviation σ of the resulting signal, and define our limit of detection as 3σ, shown in Figure S5.

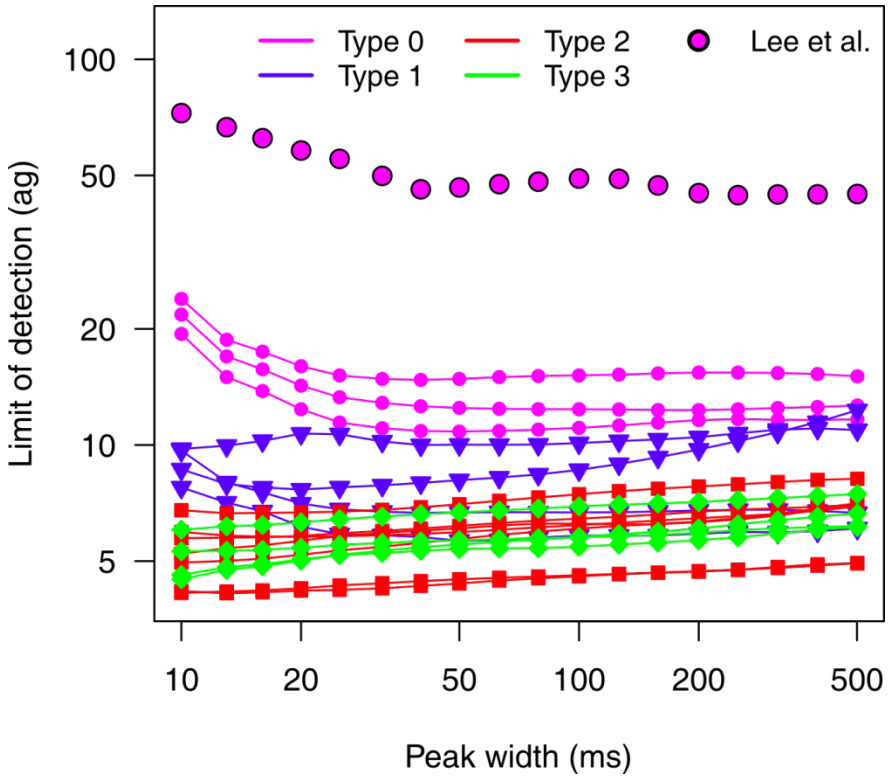

Figure S5 Limits of mass detection for the devices considered in this study. Limits of detection are calculated based on applying approximately matched filters of varying widths and calculating three times the resulting noise standard deviation. The apparent independence of limit of detection and peak width over the range from 20-500 mHz results from the dominating 1/f noise, which has equal power in every decade of the spectrum.

6 Mass Sensitivity Calibration

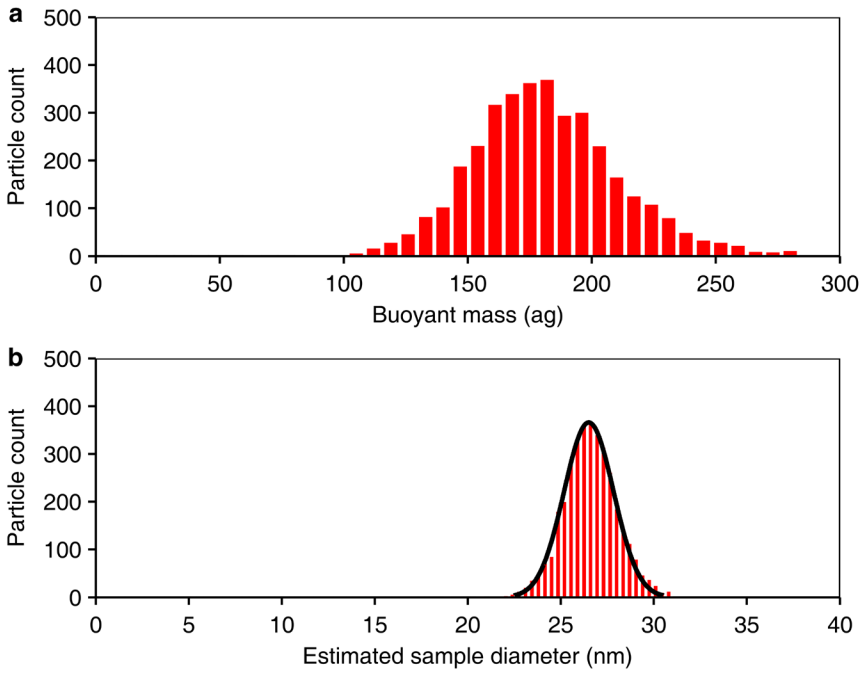

Figure S6 Mass sensitivity calibration of SNRs. We calibrated the mass sensitivity of the cantilevers by running gold nanoparticles (RM-8012, NIST) as reference before the actual experiment. We calculate the sensitivity of a cantilever such that the mean diameter of the measurement is 26.5 nm, which is the mean of the estimated diameter of the nanoparticles by AFM, SEM and TEM measurements in the reference material datasheet. **(a)** Buoyant mass histogram of reference gold nanoparticles. 3,600 particles are measured in a 20-minute experiment. **(b)** Histogram of the estimated diameter of weighed particles by assuming a spherical shape and uniform gold density of 19.3 g/cm^3.

7 Dynamic light scattering measurements of gold nanoparticles

For comparing the performance of SNRs to dynamic light scattering (DLS), we measured the gold nanoparticle populations used in the experiment given in Fig. 3 using a Malvern ZEN3690 DLS instrument. First, we analyzed 10 nm, 15 nm and 20 nm gold nanoparticles, separately. The results of the measurements are given in Table S2, below.

		DLS		SNR (from the mixture)		Datasheet	
Sample		Mean (nm)	CV(%)	Mean (nm)	CV(%)	Mean (nm)	CV(%)
1	10 nm AuNP	12.68	10.2	9.9	7.4	9.9	
2	15 nm AuNP	15.99	13.4	14.4	5.3	14.3	< 8%
3	20 nm AuNP	22.07	15.6	19.7	4.9	20.4	< 8%
4	Mixture	18.77	24.8				

Table S2 DLS measurements of the gold nanoparticles used in this work. Samples 1, 2 and 3 are monodisperse populations of gold nanoparticles used in sample 4, which was weighed in the SNR and the results were given in Fig. 3.

For the mono-disperse gold nanoparticle populations, the mean diameters measured by the DLS are slightly higher than what were measured by SNR or reported in the datasheets of the particles. The measured coefficients of variances (CV's) by the DLS are also higher than SNR measurements. More importantly, DLS detects the mixture of these particles as a single peak around 18.77 nm with a relatively broader coefficient of variance (24.8%) compared to the single particle measurements.

8 Dynamic range in size

We demonstrate the dynamic range of SNRs by weighing a mixture of equal concentration 150 nm, 200 nm and 220 nm polystyrene beads (NIST traceable Thermo Scientific). The same cantilever and detection and estimation parameters that were used for gold nanoparticle mixture that was shown in Fig. 3 were used to weigh the polystyrene nanoparticle mixture. The three populations were successfully identified by measuring more than 12,500 particles in less than 30 minutes. We estimated the average transit time for a single particle as 30 ms. The estimated diameters in Figure S7b is calculated by assuming a spherical shape and uniform polystyrene density of 1.05 g/cm^3. Calculated coefficient of variations and the mean sizes for the three populations are 2.3% around 149.8nm, 1.7% around 199.9nm and 1.2% around 217.2nm, respectively.

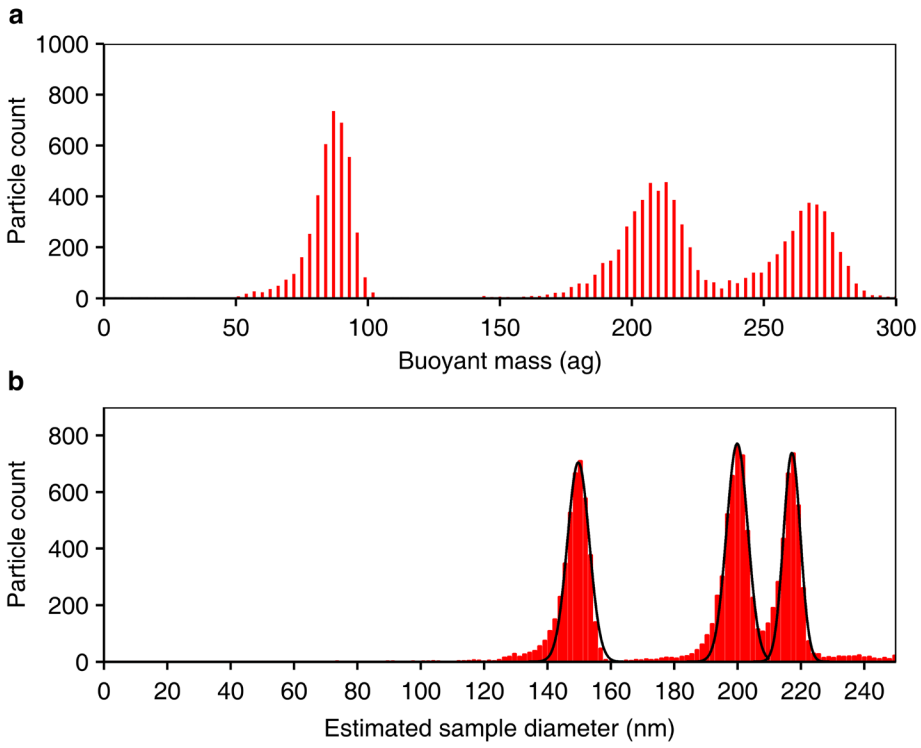

Figure S7 Dynamic range of SNRs. (a) Buoyant mass histogram of a mixed population of 150 nm, 200 nm and 220 nm polystyrene nanoparticles. **(b)** Estimated diameters of weighed nanoparticles. Black curves are Gaussian fits to the histograms.

9 Accuracy of concentration estimation

The concentration of particles in a solution is estimated by the ratio of the number of particles detected and the estimated total analyte volume. The amount of analyte flowing through the cantilever is calculated using the transit time estimates of the particles and the cantilever dimensions. Concentration accuracy is affected by the error in the particle count and the error in the estimated analyte volume.

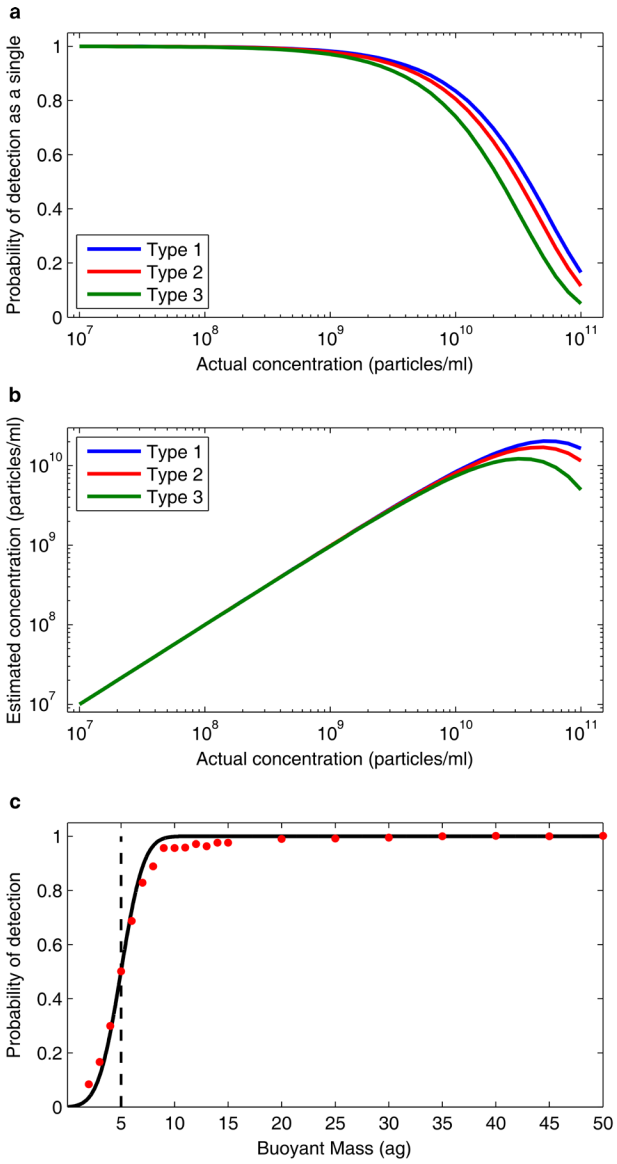

Figure S8 Accuracy of the concentration estimates. (a) Probability of a particle being detected (vs being coincident with another particle) as a function of sample concentration. **(b)** Estimated concentration as a function of actual concentration when there are no other error sources. **(c)** Probability of detection of a particle as a function of buoyant mass. The vertical dashed line is the limit of detection (5 ag) for the cantilever under consideration. The red circles are the simulation results using the detection algorithm when simulated particle peaks are inserted in real frequency noise data.

Erroneous particle counts are caused by two primary factors – coincident (overlapping) particles in the cantilever, and failure to detect particles that are close to the limit of detection. Coincidence occurs if two particles transit the cantilever close together enough that they cannot be distinguished from a single, larger particle. Here, we conservatively consider particles to be coincident if the distance between two particles in the cantilever channel is less than half the cantilever length. Using the channel dimensions and assuming particle arrival follows a Poisson process, we calculate the probability of any given particle being sufficiently spaced from its neighbors to be detected, as a function of the particle concentration (Figure S8a). This allows us to predict the relationship between actual and observed concentrations (Figure S8b). For Type 3 devices, the error in the concentration estimate of a sample with 10^{10} particles/ml is about 15%, and is higher for the longer devices.

Another contribution to the particle count error comes from the probability of detecting a particle passing through the buried channel. The probability of detection of a particle with a buoyant mass at the detection threshold given in Figure S5 is 50% due to the inherent noise of the system. We calculated the probability of detection as a function of particle buoyant mass by integrating the frequency noise distribution converted to mass around the limit of detection. For a cantilever with 5 ag limit of detection, the probability of detection as a function of the buoyant mass is given in Figure S8c. The solid line is the calculated theoretical detection probability whereas the red circles are the results of the detection of simulated particle signals superimposed on a measured noise waveform. A total of 600 particles were injected in the measured noise waveform of 10 minutes and the detection algorithm was used to detect the superimposed particle signals. The simulation results and the theoretical estimations agree well.

Estimating the flow rate of the fluid passing through the buried channel using the pressure difference across the cantilever and the channel dimensions does not provide satisfactory results since the flow rate during an experiment may vary due to partial clogging or surface adhesion. So we use the particle transit time through the cantilever as an estimate of the linear flow velocity. Coupled with the cantilever dimensions, we can use this to estimate the volumetric flow rate. To assess the accuracy of this method, we simulate the performance of our detection algorithm on estimating the transit time of the particles. We inject 600 particles with 100 ms transit time to a measured frequency noise waveform of Type 2 device with 5 ag limit of detection. As expected, the variance of the transit time estimates increases as the particle mass approaches to the limit of detection. We calculated the standard deviation of the transit time estimates as 20.5 ms around a mean of 95.2 ms for 10 ag particles. Although individual particles show a large variance the error on the mean value for 600 particles is less than 5% and gets smaller for higher number of measured particles. The variance of the transit time estimates reduces very quickly as the signal to noise ratio improves. For example, the error of transit time estimate using 100 ag particles (600 particles) is less than 1% with a standard deviation of 1.8 ms.

10 Exosome diameter estimation

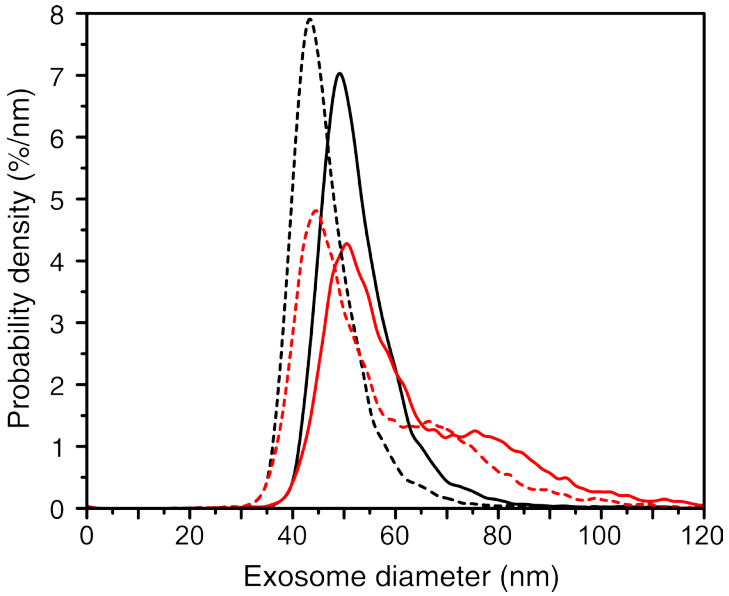

Figure S9 Estimated size distribution (kernel density estimates) of fibroblast (red) and hepatocyte (black) exosomes for different assumed exosome densities. The data used for size estimation is the buoyant mass measurements in Fig. 4. Two extreme cases for the mean exosome density are considered; 1.13 g/ml (solid), and 1.19 g/ml (dashed). All exosomes are assumed to be spherical.

11 Dynamic light scattering measurements of exosomes

We performed DLS measurements of different types of exosome populations for comparison. The mean of the dominant mode (in concentration) detected by the DLS is 44.6 nm and 44.1 nm for fibroblast and hepatocyte exosomes with standard deviations of 12.9 nm and 6.3 nm, respectively. The DLS measurements, similar to SNR measurements, estimate a broader distribution for the fibroblast exosomes compared to hepatocyte exosomes. However, DLS does not provide information about the shape of the distribution or absolute concentration. In addition, we note that the information gathered from the DLS is not very reliable for heterogeneous samples like exosomes, due to the fact that DLS is biased towards the detection of larger particles (5).

Exosomes		DLS	
		Mean (nm)	Std (nm)
1	Fibroblast	44.6	12.9
2	Hepatocyte	44.1	6.3

Table S3 DLS measurements of the exosome populations analyzed in this work. Malvern ZEN3690 DLS instrument is used for the measurements.

12 Repeated exosome measurements

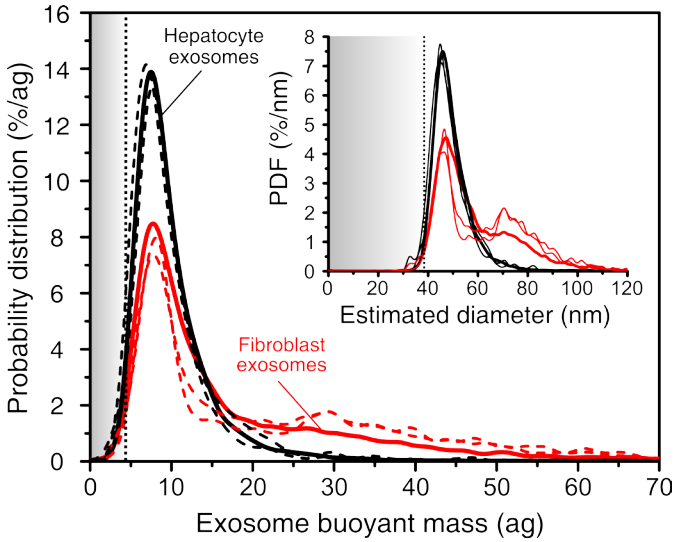

Figure S10 Distribution of buoyant mass measurements (kernel density estimates) of exosomal vesicles derived from fibroblast (red) and hepatocyte (black) cells. The thinner dashed lines are the results of the repeated measurements using a second batch of purified fibroblast and hepatocyte exosomes and using a different cantilever. The vertical line close to 5 ag depicts the limit of detection of the measurements. The inset shows the estimation of exosome diameter by assuming a spherical shape and uniform density of 1.16 g/ml.

13 Preparation of DNA covered gold nanoparticles

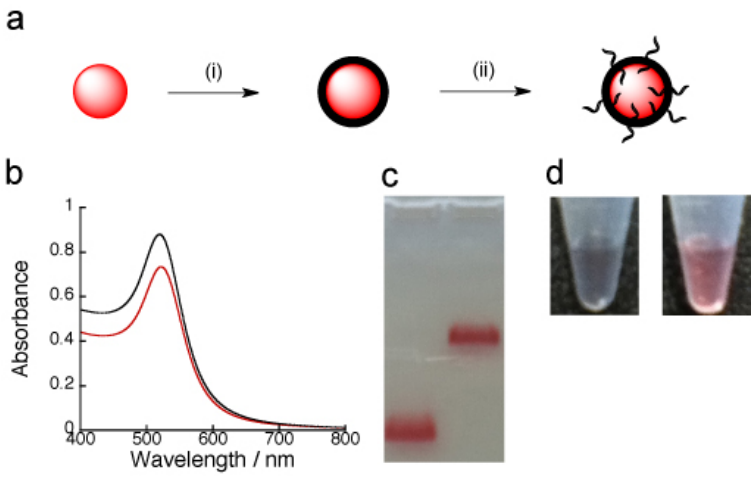

Figure S11 Preparation of DNA-covered gold nanoparticle. (a) Schematic illustration of a DNA-covered gold nanoparticle. (i) Gold nanoparticles were incubated with bis(p-sulfonatophenyl)-phenylphosphine (BSPP) at room temperature overnight. (ii) The phosphinated gold nanoparticle solution was incubated with activated thiol-DNA at room temperature overnight. **(b)** UV spectra of a bare gold nanoparticle (black, λ_{max} = 519.5 nm) and a phosphinated gold nanoparticle (red, λ_{max} = 522.5 nm). Phosphination of a gold nanoparticle causes the change of environment on its surface and λ_{max} of the phosphinated gold nanoparticle shifts by 3 nm. **(c)** Agarose gel analysis identifies phosphinated (left) and DNA-covered (right) gold nanoparticles. **(d)** A photograph of phosphinated gold nanoparticles (left) and DNA-covered gold nanoparticles (right) under high salt conditions. Gold nanoparticles not covered by DNA aggregate under high salt solution.

14 Design of DNA origami scaffold

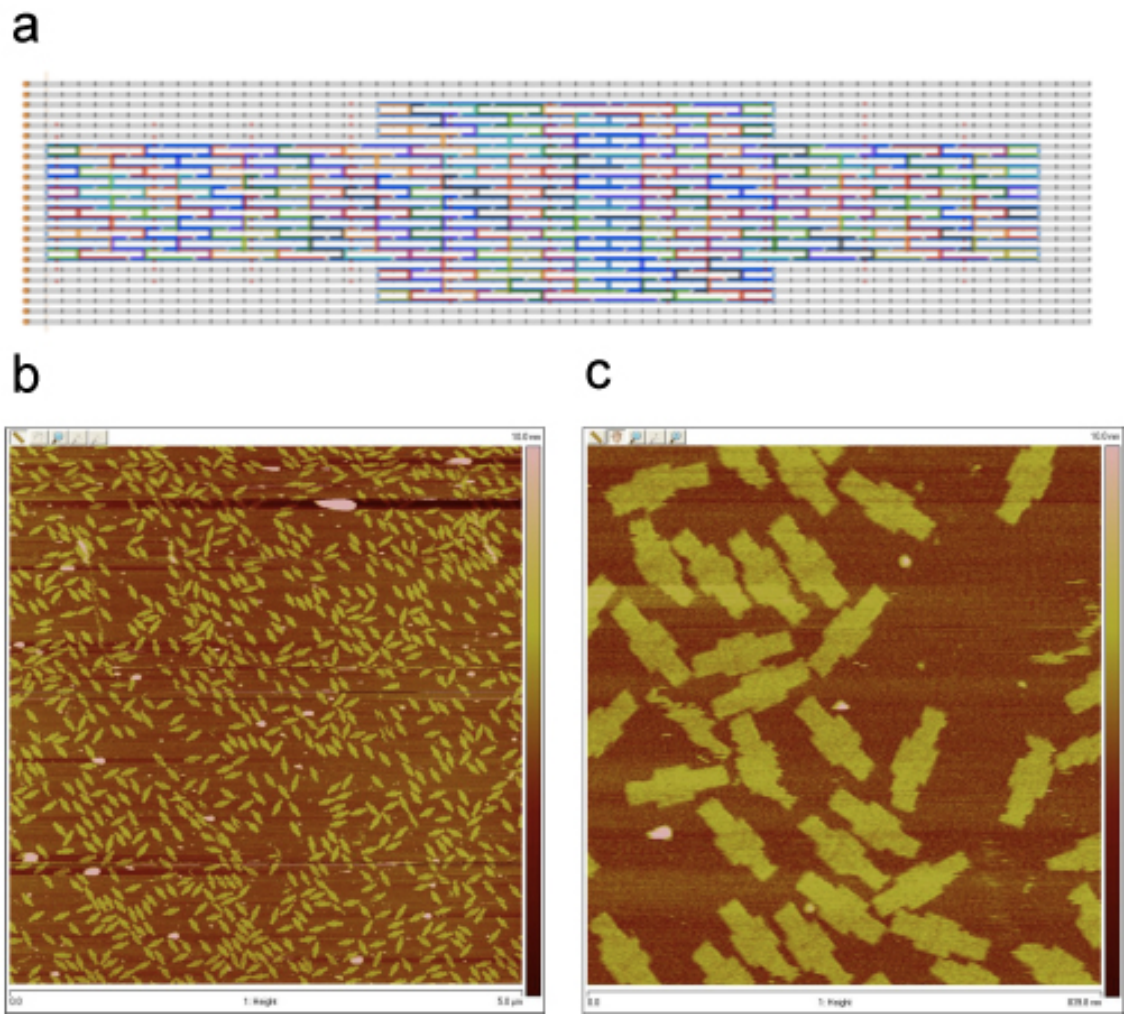

Figure S12 Design and AFM images of DNA origami scaffold. **(a)** Design of the DNA origami. Each color shows individual single stranded DNAs. The constructed DNA origami scaffold was examined by AFM. Scale: **(b)** 5.0 μm x 5.0 μm; **(c)** 839.8 nm x 839.8 nm.

15 Design and preparation of gold covered DNA origami

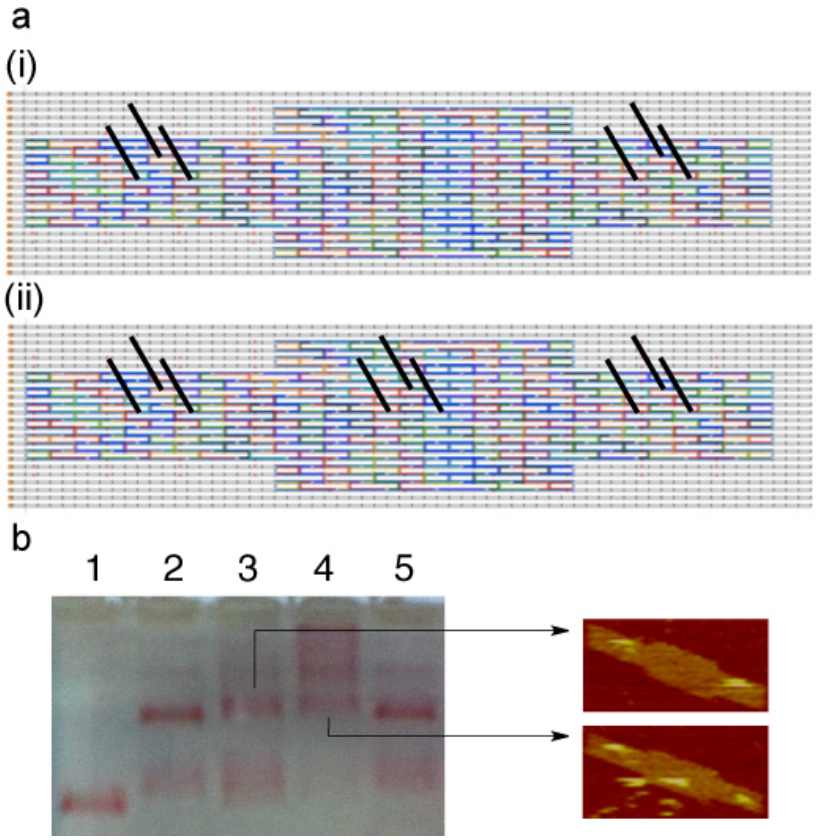

Figure S13 Design and preparation of gold nanoparticles-embedded DNA origami. (a) The design of DNA origami structures with two (i) and three (ii) binding sites for DNA-modified gold nanoparticles. **(b)** Agarose gel analysis and AFM images of the gold nanoparticles-embedded DNA origami. Annealed products of DNA origami with gold nanoparticles were loaded on 1% Sybr safe-stained agarose gel containing 10 mM $MgCl_2$ (running buffer TBE (0.5X), loading buffer 40% glycerol, 15 V/cm, 30 minutes, room temperature). Lane 1 contains 15 nm gold nanoparticles fully covered by DNA. Lane 2 contains DNA origami with one binding site and the DNA-modified gold nanoparticles. (origami:gold = 1:1) Lane 3 contains DNA origami with two binding sites and the DNA-modified gold nanoparticles (origami:gold = 1:2). Lane 4 contained DNA origami with three binding sites and the DNA-modified gold nanoparticles (origami:gold = 1:3). Lane 5 contains DNA origami with one binding site and the DNA-modified gold nanoparticle, same as lane 2. The selected bands were excised and purified for analysis using Freeze-squeeze column (Bio-Rad) at 4°C. 4 μl $NiCl_2$ (10 mM) was dropped on freshly cleaved mica. After 20 minutes, the surface was dried by nitrogen gas. 4 µl of the sample with DNA origami and gold nanoparticles was dropped on the pretreated substrate. Then the samples were scanned in TAE-Mg^{2+} (1X) buffer on AFM (Veeco Multimode with NanoScope V) in tapping mode with a SNL-10 tip (Bruker corporation). Scale: 100 nm x 200 nm.

16 DNA sequence of staple strands.

Sequence (5'-3') of staples strands used in the experiments is shown below. Gold nanoparticles embedded to DNA origami structures were prepared by substituting original staple strands (HA856, 901, 902, 851, 896, 897, 861, 906, and 907) with hook staple strands (HA1057-1065).

HA0795	GGTCATAGAATTCCACACAACATAATTGGGCG
HA0796	CCCCGGGTAAGTGTAAAGCCTGGGCGGCCAAC
HA0797	CTTGCATCTAACTCACATTAATGAAACCTG
HA0798	CACGACGTTGTAAAACGACGGCCAGTGCCAAG
HA0799	TTAAGTTGGGCTGCGCAACTGTTGCAGGAAGA
HA0800	TTACGCCAGCTGGCGCGGGCCTCTTCGCTA
HA0801	ATTGTTATCCGCTCACCTGTTTCCTGTGTGAA
HA0802	GAAGCATAACCGAGCTCGAATTCGTAATCAT
HA0803	TGAGTGAGGCCTGCAGGTCGACTCTAGAGGAT
HA0804	GCTCACTGGGAAACCAGGCAAAGCCACCGCTT
HA0805	CCATTCAGGTAACGCCAGGGTTTTCCCAGT
HA0806	GATCGGTGAAAGGGGGATGTGCTGCAAGGCGA
HA0807	CCAGGGTGCTGATTGCCCTTCACCGTCCACTA
HA0808	GCGCGGGGAGTTGCAGCAAGCGGTGGGTTGAG
HA0809	TCGTGCCCAGCAGGCGAAAATCCCCTTATA
HA0810	CTGGTGCCCCCGCTTTCCAGTCGGTGCGTTGC
HA0811	TCGCACTCGATAGGTCACGTTGGTTTTCATCA
HA0812	CAGTTTGAGGGGACGTAACCGTGCATCTGC
HA0813	GTGAGACGGGCAACAGGTTTTTCTTTTCACCA
HA0814	CCTGAGAGAGAGGCGGTTTGCGTCGAGCCG
HA0815	GTTTGCCCAGCTGCATTAATGAATGTGCCTAA
HA0816	TGGTGGTTGTGGGAACAAACGGCGACCCGTCG
HA0817	GTAATGGCAGCCAGCTTTCCGGGCCATTCG
HA0818	GCGCATCGACGACAGTATCGGCCTGGAAGGGC
HA0819	CCCGCCGCTGGTTGCTTTGACGAGCGCGAACT
HA0820	TGTAGCGTCCTCGTTAGAATCAAATATTTT
HA0821	GCGAAAGGGGAGGCCGATTAAAGGGACCTGAA
HA0822	GGCGAACGCGGTACGCCAGAATCCACATTCTG
HA0823	AAAAACCAATCAGTGAGGCCACTTCACCAG
HA0824	TTAAAGAATCCATCACGCAAATTAATCGTCTG
HA0825	TGTTGTTCCTTCTTTGATTAGTAAGCTCATGG
HA0826	AATCAAAAGTAGAAGAACTCAATATTACCG
HA0827	GATTCTCCCCGAAATCGGCAAAATCTGTTTGA
HA0828	ACATTAAATGATATTCAACCGTTCAAATGCAA
HA0829	GCGTCTGGGCCGGAGAGGGTAGCGATAAAA
HA0830	TAACCAATACAAAGGCTATCAGGTTTTTGCGG
HA0831	CATTAAATTGGAGCAAACAAGAGATTGTACCA
HA0832	AATTGTAACGTAAAACTAGCATGAATAAAG
HA0833	AAGCCCCAAAAACAGGCGGTTGATAATCAGAA
HA0834	ACAGGGCGCGTACTAGCTTAATGCGCCGCT
HA0835	ACGTGCTTGTCACGCTGCGCGTAACCACCACA
HA0836	GCTAAACAAGCGGGCGCTAGGGCGCTGGCAAG
HA0837	GACAGGAATGGCGAGAAAGGAAGGGAAGAAA
HA0838	GTTTTTATGTCTATCACTTGACGGGGAAAGCC
HA0839	AGAGTCTGCGTGGACTCCAACGTCAAAGGGCG
HA0840	TAGCAATACAGTTTGGAACAAGAGCCTGGC
HA0841	CTTGCCTGAGAATAGCCCGAGATACCACGCTG
HA0842	CCTTGCTGAAGGCCGGAGACAGTCATTCAAAA
HA0843	ATCAATATGTGAGCGAGTAACAGATTGACC
HA0844	AAATTAATCCTTCCTGTAGCCAGCGTAGATGG
HA0845	AGAGATCTAGGAACGCCATCAAAAATAATTC
HA0846	GAGAGTCTTTTGTTAAATCAGCTCATTTTT
HA0847	ACGGTAATACGTTAATATTTTGTTAAAATTCG
HA0848	ATGTACCCAAGATTGTATAAGCAAATATTTA
HA0849	GATAGCCCACCACCAGCAGAAGATATCAAAAT
HA0850	TGAATGGGGTCAGTATTAACACTCTGAATA
HA0851	AGCGTAAGACGCTGAGAGCCAGCAATCAATAT
HA0852	GCCAACAGAAAGCATCACCTTGCTCATATTCC
HA0853	TCACACGACCCTCAATCAATATAAGAAACC
HA0854	AAATGGATTCAACAGTTGAAAGGAAAGTTTGA
HA0855	AAATACCTCTAAAATATCTTTAGGAAATCCTT
HA0856	CCAGCCAAGATTAGAGCCGTCAAGACTTTA
HA0857	GGGTGAGAGTAATATCCAGAACAAACTATCGG
HA0858	TGCCTGAGATTCCATATAACAGTTAGAGCTTA
HA0859	ATTTTTAGAACGAGTAGATTTAGTTTGATA
HA0860	GAGAAGCCATTTCGCAAATGGTCAGTCAGGAT
HA0861	AAAACATTATATTTTCATTTGGGGAGCGAACC
HA0862	CCTCAGAGGGCATCAATTCTACTTTCAAAT
HA0863	ACAGGCAAGGCAAAGAACATCCAATAAATCAT
HA0864	AAAAATACCGAACGATAAAACATCGCCATT
HA0865	GGTGAGGCCTATTAGTCTTTAATGCACGTATA
HA0866	ACAGTGCCAATACGTGGCACAGACGAGCGGGA
HA0867	AAAAATCTAGATAGAACCCTTCTGATTTTA
HA0868	AATATCAAACCAGTAATAAAAGGGTGAGAAGT
HA0869	TTGGCAAATATTTACATTGGCAGACGAGTAAA
HA0870	AAGGTTATACATTTTGACGCTCAACCGTTG
HA0871	CAACTAATTTGCAACAGGAAAAACTAACATCA
HA0872	TACATTTGATGCAACTAAAGTACGTCAACATG
HA0873	AAGTTTCTAATGTGTAGGTAAAGAAATCACC
HA0874	ATTCTGCGAACCCTCATATATTTTTAGCTGAT
HA0875	TTAGATACTTTATTTCAACGCAAGTATTTTTG
HA0876	TTTAGCTATGACCCTGTAATACCATTGCCT
HA0877	GAAAAGGTCATAAAGCTAAATCGGATCGATGA
HA0878	TAGCATTAATTAGCAAAATTAAGCTCAATCAT
HA0879	TATTTGCATTTTCAGGTTTAACGTTATTTTAG
HA0880	ATGGAAGAACAGTACCTTTTACGACAAAGA
HA0881	AATCCTGAACGGATTCGCCTGATTATATGTAA
HA0882	TGATTATCTTACAAAATCGCGCAGTAACCTCC
HA0883	ACCAGAATCAATTACCTGAGCATCAAAATC
HA0884	GTAACATTCAAACATCAAGAAAACTAAGACGC
HA0885	TGCCCGAATAACAATTTCATTTGAGAATCCTT
HA0886	CAAACAAGAAACAGTACATAAATAAATCGT
HA0887	TTTTAAATAGGATTTAGAAGTATTATAGATAA
HA0888	ATTGCTGAAGAGGGGGTAATAGTAAACACTAT
HA0889	AGAGGTCATAGCGTCCAATACTGGCCAAAA
HA0890	TAGAGAGTATTCATTGAATCCCCCAATACCAC
HA0891	AGACCGGAAGTTCAGAAAACGAGAAGGTAGAA
HA0892	ATCGCGTTAATCAGGTCTTTACCATAAAAC
HA0893	CATCAAAAAGATTAAGGAAGCAAAGCGGATTG
HA0894	AAGAAATTGCGTAGACGTAAAACAGAAATA
HA0895	TATACAGTGGTTAGAACCTACCATAAAACAGA
HA0896	AAACAATATTGTTTGGATTATACTCGCCTGCA
HA0897	ATACCAAGAGATGATGGCAATTCGCAAATG
HA0898	TATTCATTGGAGCGGAATTATCATGAACCTCA
HA0899	TGATGAAAATCATTTTGCGGAACACTGGTCAG
HA0900	ATTACATTCGTTATTAATTTTAAATTGAGG
HA0901	TTTTAATGTTCGACAACTCGTATTAGCACTAA
HA0902	TGTGAGTGAGCGAGAGGCTTTTGCCGATAAAA
HA0903	TTTTGCCATATAATGCTGTAGCGTGTCTGG
HA0904	AGACTGGATTTTTGCGGATGGCTTGATTCCCA
HA0905	TCATAAATACCTTTAATTGCTCCTTTTGACCA
HA0906	TTTAAACAGCAAACTCCAACAGATAACCTG
HA0907	AAATCAAATTAATTCGAGCTTCAACGCGAGCT
HA0908	TATAGTCAAGGAAGCCCGAAAGACAATAGTAG
HA0909	TTAATTTCTACCGACCGTGTGATAGCAAGCAA
HA0910	ACGCGAGAGAATAAACCACCGGATTCATCGT
HA0911	ATGCTGATAAAGCCTGTTTAGTATCACTCATC
HA0912	GGCTTAGGAATTCTTACCAGTATAATTCCAAG
HA0913	ATAGGTCGTAGGGCTTAATTGAACCAATCA
HA0914	TGAGAAGACAACGCCAACATGTAAAATATCCC
HA0915	GAAAACATTTTCGAGCCAGTAATACAACAATA
HA0916	CGCTATTCGACAAAAGGTAAAGTGTTCAGC
HA0917	ACCAAAATAATAACCTTGCTTCTGTCAATATA
HA0918	CATAACCCGAACCGGATATTCATTCTTTGAAA
HA0919	GGAATTACCAAAGCTGCTCATTCCGGTCAA
HA0920	ATTCAACTCCTGACGAGAAACACCCTCCATGT
HA0921	AGATTCATTTGGGCTTGAGATGGTCCTGATAA
HA0922	GAACTAACTCATTGTGAATTACCAAACAAA
HA0923	AGTCAGGACGTTGGGAACTGGCTCATTATACC
HA0924	TTTAATGGTTTGAAAATCTTCTGACCTAAA
HA0925	GTTAAATAAAAACTTTTTCAAATACAGATGAA
HA0926	TACTAGAAGCAAATCCAATCGCAAATCGGGAG
HA0927	GTTATACATTGGGTTATATAACTGCTTTGA
HA0928	GCTCAACATGAGAGACTACCTTTTAGGCGAAT
HA0929	ATATTTAAGTCAATAGTGAATTTAAAAGAAGA
HA0930	AGAGGCATAGCGATAGCTTAGATAAAATTA
HA0931	TAAAGTACAATTAATTTTCCCTTAATTACCTT
HA0932	TCCAGACGGGCTGACCTTCATCAAACCAGGCG
HA0933	TTGACAATCGTTTACCAGACGAAAAAGAAG
HA0934	CAACGTAAGAGGCATAGTAAGAGCAAATGTTT
HA0935	AGGCTTGCAATGCAGATACATAACCGGAATCG
HA0936	TAGTAAACAGTTGAGATTTAGGTCAAATGC
HA0937	AACTTTAAGGAACAACATTATTACATGACCAT
HA0938	TTTTAAGAAGAAAAATCTACGTTACTGACTAT
HA0939	ATCAGATAGAGGCGTTTTAGCGAAAAAAGAAC
HA0940	AGGAATCAGGTTTTGAAGCCTTACCGAGGA
HA0941	GAGAACAACTATTTTGCACCCAGCAGCAGATA
HA0942	AACGGGTAAATCTTACCAACGCTATATCTTAC
HA0943	ATAATCGAGCCTAATTTGCCAGTAAGAGCA
HA0944	ATCCTAATCATATTATTTATCCCAATAACCCA
HA0945	GATAAGTCGATTTTTTGTTTAACGCAGAGGGT
HA0946	TAATGCACAGCCTTTACAGAGAGGGAGAAT
HA0947	CATAGGCTACGACAATAAACAACATAATTCTG
HA0948	GAGGACAGTCACCCTCAGCAGCGAACAACCAT
HA0949	TCATAAGGGAGGGTAGCAACGGCCTTGATA
HA0950	TACTTAGCACTAAAGACTTTTTCACAGCTTGC
HA0951	ATTGTGTCTAAACGGGTAAAATACCCAAAAGG
HA0952	GTACAACGGGCACCAACCTAAAATTTCACG
HA0953	ATCTTTGACCCCCAGCATACACTAAAACACTC
HA0954	GTATTCTAAGAACGCTAGAAGGCTTATCCG
HA0955	CTTGCGGGATTACCGCGCCCAATAAATAAGGC
HA0956	ATTAGTTGGCAAGCCGTTTTTATTATCATAAT
HA0957	TTATCCTGTTAAACCAAGTACCGCATATGC
HA0958	CTTTCCAGGCTGTCTTTCCTTATCAAGCCAAC
HA0959	TAAACAGCTTACGAGCATGTAGAAGAATCGCC
HA0960	TAAGAAACCTGAACAAGAAAAATTTTAGGC
HA0961	GAAAATAGGAACGCGCCTGTTTATAGAGAATA
HA0962	TAAAAACACAGGGAGTTAAAGGCCCGGTCGCT
HA0963	GGGATCGATGAACGGTGTACAGGAGTAATC
HA0964	ATCGGAACGAACCGAACTGACCAAACCCAAAT
HA0965	CTTTGAGGCGGAACGAGGCGCAGAAGTGAATA
HA0966	TTTCCATGAAATCCGCGACCTGAGAACGAG
HA0967	ACTACGAAGAGATTTGTATCATCGTTAATTTC
HA0968	GCAAAAGAGATTATACCAAGCGCGTTATGCGA
HA0969	TGGCATGAAAACGTAGAAAATACATACATAAA
HA0970	AACGCAACATATAAAAGAAACGCAAAGACA
HA0971	GCCGAACATAAGTTTATTTTGTCACAATCAA
HA0972	CGAAGCCCTCATATGGTTTACCAGCGCCAAAG
HA0973	AGAAACAGCGACATTCAACCGATTGAGGGA
HA0974	CAAGAATTAAATATTGACGGAAATGTTTGCCT
HA0975	AATTGAGCAATTATCACCGTCACCGCAGCACC
HA0976	TAACTGAGAATTAGAGCCAGCAGCCGGAAA
HA0977	GAGGCTTGGGGAAGCGCATTAGACGAATAACA
HA0978	CGCCCACGACTGAGTTTCGTCACCCCTCAGAA
HA0979	CCGATAGTCCTGTAGCATTCCACAGACAGCC
HA0980	TTTCGAGGTAGCGTAACGATCTAAAGTTTTGT
HA0981	AGCCTTTACCAGACGTTAGTAAATGAATTTTC
HA0982	TTGAAAATATTTTGCTAAACAACTTTCAACA
HA0983	GGAACAACTAAAGGAAGGAGTGAGAATAGAAA
HA0984	ACGCAGTATGTTAGCTTAAGACTCCTTATT
HA0985	GGTGGCAATAATAACGGAATACCCCCTCCCGA
HA0986	CCACGGAAAAGTTACCAGAAGGAAAAATCAAG
HA0987	TAGAAAATTTTTTAAGAAAAGTATACAATT
HA0988	ACAAAAGGATGAAATAGCAATAGCACGAGCGT
HA0989	GGGAAGGTGAGTTAAGCCCAATAATTACAAAA
HA0990	TAAAGGTGGCTAATATCAGAGAGATCCAAA
HA0991	CCATTTGGACACCCTGAACAAAGTTCAAAAAT
HA0992	AGTAGCACGCAAGCCCAATAGGAACTCATTTT
HA0993	CCGTAACCATAACCGATATATTGCTTTTGC
HA0994	CTACAACGTGCGCCGACAATGACAAAGACAGC
HA0995	CTCATAGTTGAATTTCTTAAACAGTACAGAGG
HA0996	CGTCTTTATTGTATCGGTTTATTGAGGAAG
HA0997	TGTATGGGCTCCAAAAAAAAGGCTGTAATGCC
HA0998	GTTTCAGCTTGCGAATAATAATTTCGAAAGAG
HA0999	TTAGCGTCTCATAGCCCCCTTATTAGGAGGTT
HA1000	GTAATCAGTTCATAATCAAAATCAAACCACCA
HA1001	CGTCACCCACCGGAACCGCCTCTCAGAGCC
HA1002	CAGGGATACATTACCATTAGCAAGAAATCACC
HA1003	CCGCCACCGGTTGATATAAGTATAGAGGCTGA
HA1004	GGTTTAGTACCGCCATCACCGTACTCAGGA
HA1005	TCATCGGCATTTTTCGGAGACTGTAGCGCGTTT
HA1006	GCCATCTTTAGCGACAGAATCAATATTCAT
HA1007	AGAGCCACAATGAAACCATCGATAGACTTGAG
HA1008	CCGCCACCTCAGTACCAGGCGGATATTAGCGG
HA1009	TCGAGAGCTCAGAGCCACCACCCCCATGTA
HA1010	TAGGTGTACCCTCAGAACCGCCACAGTACAAA
HA1011	GAGGCAGGTAAATCCTCATTAAAGCCAGAAT
HA1012	CCAGAGCCCAGTCTCTGAATTTACCGTTCCAG
HA1013	ACCACCCATACATGGCTTTTGATGATACAG
HA1014	GGTTTTGCCTCAGAACCGCCACCCCCTCAGAG
HA1015	GACTCCTCGAGTAACAGTGCCCGTATAAACAG
HA1016	AACCTATTATTCTGACCCTGCCTATTTCGG
HA1017	GATATTCACAAACAAATCAGACGATTGGCCTT
HA1018	GGAAAGCGGCCGCCAGCATTGACAGCGTTT
HA1019	TAAGCGTCTCAGAGCCGCCACCAGCCGGAACC
HA1020	GAGTGTACTGGTAATAAGTTTTAACGGGGTCA
HA1021	GTGCCTTAAGAGAAGGATTAGGAAGTGCCG
HA1022	TTAATGCCAACATGAAAGTATTAAGCCCGGAA
HA1056	AAAAAAAAAAAAAAAAAAAAAAAAAATTTTCCAGC CAAGATTAGAGCCGTCAAGACTTTA
HA1057	AAAAAAAAAAAAAAAAAAAAAAAAATTTTTTTT AATGTTCGACAACTCGTATTAGCACTAA
HA1058	AAAAAAAAAAAAAAAAAAAAAAAAATTTTTGTG AGTGAGCGAGAGGCTTTTGCCGATAAAA
HA1060	AAAAAAAAAAAAAAAAAAAAAAAAATTTTAGCG TAAGACGCTGAGAGCCAGCAATCAATAT
HA1061	AAAAAAAAAAAAAAAAAAAAAAAAATTTTAAAC AATATTGTTTGGATTATACTCGCCTGCA
HA1062	AAAAAAAAAAAAAAAAAAAAAAAAAATTTTATAC CAAGAGATGATGGCAATTCGCAAATG
HA1063	AAAAAAAAAAAAAAAAAAAAAAAAAATTTTAAAA CATTATATTTTCATTTGGGGAGCGAACC
HA1064	AAAAAAAAAAAAAAAAAAAAAAAAATTTTTTTA AACAGCAAACTCCAACAGATAACCTG
HA1065	AAAAAAAAAAAAAAAAAAAAAAAAATTTTAAAT CAAATTAATTCGAGCTTCAACGCGAGCT

17 References

1. Albrecht TR, Grütter P, Horne D, Rugar D (1991) Frequency modulation detection using high-Q cantilevers for enhanced force microscope sensitivity. *J Appl Phys* 69:668–673.

2. Arlett JL, Roukes ML (2010) Ultimate and practical limits of fluid-based mass detection with suspended microchannel resonators. *J Appl Phys* 108.

3. Cleland AN, Roukes ML (2002) Noise processes in nanomechanical resonators. *J Appl Phys* 92:2758–2769.

4. Dohn S, Svendsen W, Boisen A, Hansen O (2007) Mass and position determination of attached particles on cantilever based mass sensors. *Rev Sci Instrum* 78:103303–103303–3.

5. Van Der Pol E et al. (2010) Optical and non-optical methods for detection and characterization of microparticles and exosomes. *J Thromb Haemost* 8:2596–2607.